

Magnetic phase transitions in $\text{Eu}(\text{Co}_{1-x}\text{Ni}_x)_{2-y}\text{As}_2$ single crystals

N. S. Sangeetha,¹ Santanu Pakhira,¹ D. H. Ryan,² V. Smetana,³ A.-V. Mudring,³ and D. C. Johnston^{1,4}

¹Ames Laboratory, Ames, Iowa 50011, USA

²Physics Department and Centre for the Physics of Materials,
McGill University, 3600 University Street, Montreal, Quebec, H3A 2T8, Canada

³Department of Materials and Environmental Chemistry,

Stockholm University, Svante Arrhenius väg 16 C, 106 91 Stockholm, Sweden

⁴Department of Physics and Astronomy, Iowa State University, Ames, Iowa 50011, USA

(Dated: March 14, 2024)

The effects of Ni doping in $\text{Eu}(\text{Co}_{1-x}\text{Ni}_x)_{2-y}\text{As}_2$ single crystals with $x = 0$ to 1 grown out of self flux are investigated via crystallographic, electronic transport, magnetic, and thermal measurements. All compositions adopt the body-centered-tetragonal ThCr_2Si_2 structure with space group $I4/mmm$. We also find 3–4% of randomly-distributed vacancies on the Co/Ni site. Anisotropic magnetic susceptibility χ_α ($\alpha = ab, c$) data versus temperature T show clear signatures of an antiferromagnetic (AFM) c -axis helix structure associated with the Eu^{+2} spins-7/2 for $x = 0$ and 1 as previously reported. The $\chi_\alpha(T)$ data for $x = 0.03$ and 0.10 suggest an anomalous $2q$ magnetic structure containing two helix axes along the c axis and in the ab plane, respectively, whereas for $x = 0.75$ and 0.82, a c -axis helix is inferred as previously found for $x = 0$ and 1. At intermediate compositions $x = 0.2, 0.32, 0.42, 0.54$, and 0.65 a magnetic structure with a large ferromagnetic (FM) c -axis component is found from magnetization versus field isotherms, suggested to be an incommensurate FM c -axis cone structure associated with the Eu spins, which consists of both AFM and FM components. In addition, the $\chi(T)$ and heat capacity $C_p(T)$ data for $x = 0.2$ –0.65 indicate the occurrence of itinerant FM order associated with the Co/Ni atoms with Curie temperatures from 60 to 25 K, respectively. Electrical resistivity $\rho(T)$ measurements indicate metallic character for all compositions with abrupt increases in slope on cooling below the Eu AFM transition temperatures. In addition to this panoply of magnetic transitions, ^{151}Eu Mössbauer measurements indicate that ordering of the Eu moments proceeds via an incommensurate sine amplitude-modulated structure with additional transition temperatures associated with this effect.

I. INTRODUCTION

Many RM_2X_2 (abbreviated as 122-type) ternary compounds (R = rare-earth or alkaline-earth metal, M = transition metal, X = pnictogen), crystallize in the body-centered tetragonal ThCr_2Si_2 structure with space group $I4/mmm$. They have been widely investigated owing to a variety of remarkable physical properties such as unconventional superconductivity, heavy fermion behavior, valence fluctuations, quantum criticality, and different types of magnetic transitions [1–10]. The 122-type compounds are quite sensitive to the peculiarities of electronic band structure and the Fermi surface. In particular, tuning the system either by external stimuli (pressure, temperature) or chemical substitution leads to a variety of ground states [11–21]. For example, EuFe_2As_2 exhibits localized Eu^{+2} spin-7/2 A-type antiferromagnetism below 19 K and an itinerant antiferromagnetic (AFM) spin-density-wave (SDW) ordering accompanied by a tetragonal-to-orthorhombic structural phase transition below 190 K. Superconductivity can be induced in EuFe_2As_2 by suppressing the SDW ordering either by chemical substitution or by applying external pressure [22–28].

The ThCr_2Si_2 -type Co pnictides EuCo_2P_2 and $\text{EuCo}_{2-y}\text{As}_2$ have also attracted considerable attention. EuCo_2P_2 has an uncollapsed-tetragonal (ucT) structure [29]. It shows AFM ordering below $T_N = 66$ K on the Eu^{+2} sublattice and there is no evident contribution

to the ordering from the Co atoms at ambient pressure [30]. Neutron-diffraction studies demonstrated that the AFM structure is a planar helix with the Eu ordered moments aligned in the ab plane of the tetragonal structure, and with the helix axis being the c axis with propagation vector $\mathbf{k} = (0, 0, 0.85)(2\pi/c)$ [31]. This compound undergoes a pressure-induced first-order ucT to collapsed-tetragonal (cT) transition at ≈ 3 GPa [32]. ^{151}Eu high-pressure Mössbauer experiments ($0 \leq p \leq 5$ GPa) [33] reveal a valence transition of Eu from Eu^{+2} with spin $S = 7/2$ and angular momentum $L = 0$ to nonmagnetic Eu^{+3} (7F_0) at $p = 3$ GPa together with emergence of itinerant $3d$ magnetism on the Co sublattice which orders antiferromagnetically at $T_N^{\text{Co}} = 260$ K. The unique feature of EuCo_2P_2 is that it changes its magnetic character from Eu($4f$) ordering to Co($3d$) ordering depending on its lattice parameter. For this reason, EuCo_2P_2 is a model system for band-structure calculations studying $3d$ moment formation in the ThCr_2Si_2 -type structure [33]. We showed that EuCo_2P_2 is a textbook example of a non-collinear helical antiferromagnet at ambient pressure for which the thermodynamic properties in the antiferromagnetic (AFM) state are well described [34] by our recent formulation of molecular field theory (MFT) [35, 36].

$\text{EuCo}_{2-y}\text{As}_2$ is isostructural and isoelectronic to EuCo_2P_2 and exhibits AFM ordering of the Eu^{+2} spins-7/2 below $T_N = 47$ K [22, 37–41]. Neutron-diffraction measurements revealed that the AFM structure is the same coplanar c -axis helical structure as in EuCo_2P_2 with

propagation vector $\mathbf{k} = (0, 0, 0.79)(2\pi/c)$ and no evident participation of Co in the ordering [40].

It is interesting to note the differences between EuCo_2P_2 and $\text{EuCo}_{2-y}\text{As}_2$ as a consequence of their different Co-P and Co-As networks. Their c/a ratios are similar, 3.01 for EuCo_2P_2 and 2.93 for $\text{EuCo}_{2-y}\text{As}_2$. However, $\text{EuCo}_{2-y}\text{As}_2$ exhibits a continuous ucT to cT transition under applied pressure $p \approx 5$ GPa that leads to an intermediate-valence state $\text{Eu}^{+2.25}$ at 12.6 GPa [38]. As a result, the electronic structure change eliminates the AFM ordering of the Eu spin sublattice and ferromagnetic (FM) ordering then arises in which both Eu (4*f*) and Co (3*d*) moments participate with a Curie temperature $T_C = 125$ K, as confirmed by x-ray magnetic circular dichroism measurements and electronic structure calculations [40].

Conventionally, the paramagnetic (PM) effective moment of Eu^{+2} with spin $S = 7/2$ and spectroscopic splitting factor $g = 2$ is calculated to be $\mu_{\text{eff}} \approx 7.94 \mu_B/\text{Eu}$. Instead, crystals of the helical antiferromagnet $\text{EuCo}_{2-y}\text{As}_2$ exhibit an enhanced effective moment $\mu_{\text{eff}} \approx 8.5 \mu_B/\text{Eu}$, where μ_B is the Bohr magneton [41]. This enhancement is consistent with the occurrence of an enhancement of the low- T ordered moment to $7.26(8)\mu_B$ found in the neutron diffraction study [40]. *Ab initio* calculations showed that the enhancements arise from FM polarization of the conduction electron spins around each Eu spin [41]. This was the second example of a helical antiferromagnet with thermal and magnetic properties that are fitted rather well by MFT [35, 36]. In Ref [41], we also found a Co vacancy concentration up to $y = 0.1$ in $\text{EuCo}_{2-y}\text{As}_2$.

Studies of ^{153}Eu , ^{75}As , and ^{59}Co NMR were also carried out on a crystal of $\text{EuCo}_{2-y}\text{As}_2$ [42], where NMR signals from all three isotopes were observed. From the applied magnetic field dependence of the ^{153}Eu and ^{75}As NMR spectra at low temperature $T \ll T_N = 45$ K, the signals were consistent with an incommensurate helical AFM structure with propagation vector $[0, 0, 0.73(7)]2\pi/c$, which is the same within the errors as the propagation vector found from the above neutron-diffraction experiment [40]. In addition, from the ^{59}Co NMR it was determined that the Co atoms do not participate in the AFM ordering, again consistent with the conclusion from the neutron-diffraction measurements [40]. The temperature dependence of the ^{75}As hyperfine field below T_N was fitted quite well by a Brillouin function for spin $S = 7/2$.

The electron-doped analog $\text{EuNi}_{2-y}\text{As}_2$ of $\text{EuCo}_{2-y}\text{As}_2$ is metallic and from magnetic susceptibility and heat-capacity measurements exhibits an AFM transition at $T_N \approx 14\text{--}15$ K [43–46]. The electron doping is inferred from the fact that Ni has one more 3*d* electron than Co does. This compound has recently been found from neutron-diffraction measurements to have a c -axis helical AFM structure with $T_N = 15$ K and AFM propagation vector $k = (0, 0, 0.9200)2\pi/c$, corresponding to a turn angle of $165.6(1)^\circ$ along the c axis

between adjacent layers of Eu spins ferromagnetically aligned in the ab plane [45].

We subsequently reported a comprehensive study of the properties of single crystals of $\text{EuNi}_{2-y}\text{As}_2$ [46], where the analysis of the anisotropic magnetic susceptibility χ data below T_N by MFT yielded a c -axis helical turn angle in good agreement with the neutron-diffraction result. In addition, a 2.5% vacancy concentration on the Ni sites was detected. A good fit of the electrical resistivity $\rho(T)$ by the Bloch-Grüneisen electron-phonon scattering theory was obtained. The magnetic contribution to the heat capacity $C_p(T)$ below T_N was compared with the MFT prediction. The ab -plane isothermal magnetization $M_{ab}(H)$ exhibited two metamagnetic transitions in fields up to $H = 14$ T at $T = 2$ K, whereas $M_c(H)$ was linear up to the critical field, both in agreement with MFT. A review of the crystallographic and magnetic properties of ThCr_2Si_2 -type pnictides (Pn) EuM_2Pn_2 was also presented in Ref. [46] in which only ferromagnetic and c -axis helical AFM structures are found to be present. Here, an A-type antiferromagnet with FM ab -plane ordered-moment alignment was considered to be a c -axis helix with a 180° turn angle between the ordered moments in adjacent ab -plane layers.

In this work we report a comprehensive single-crystal study of the mixed system $\text{Eu}(\text{Co}_{1-x}\text{Ni}_x)_{2-y}\text{As}_2$ including the crystallographic, magnetic, thermal, and electronic-transport properties obtained using single-crystal x-ray diffraction (XRD), $\chi(T)$, $M(H)$, ^{151}Eu Mössbauer, $C_p(T)$, and $\rho(T)$ measurements. Our major results are the discoveries of itinerant FM ordering associated with the Co/Ni spins and of a structure with both FM and AFM components at intermediate compositions from $M(H)$, $\chi(T)$, and $C_p(T)$ measurements that we suggest is an Eu-spin cone phase, and the discovery of unexpected magnetic behaviors on approaching T_N in both undoped and Ni-doped $\text{Eu}(\text{Co}_{1-x}\text{Ni}_x)_{2-y}\text{As}_2$ from ^{151}Eu Mössbauer measurements.

The experimental details are given in Sec. II. The crystallographic data and composition analyses are presented in Sec. III. The low-field $M(H)$ and the $\chi(T)$ data are presented and analyzed in Sec. IV, high-field $M(H)$ isotherms in Sec. V, ^{151}Eu Mössbauer measurements in Sec. VI, the $C_p(T)$ data in Sec. VII, and the $\rho(T)$ measurements in Sec. VIII. Concluding remarks are given in Sec. IX.

II. EXPERIMENTAL DETAILS

Single crystals of $\text{Eu}(\text{Co}_{1-x}\text{Ni}_x)_{2-y}\text{As}_2$ with measured compositions $x = 0, 0.03, 0.10, 0.20, 0.32, 0.42, 0.54, 0.65, 0.75, 0.82$, and 0.93 were grown using self-flux. The starting materials were high-purity elemental Eu (Ames Laboratory) and Co (99.998%), Ni (99.999%) and As (99.99999%) (Alfa Aesar). The sample and flux were taken in a Eu : $4(1-x)$ CoAs : $4x$ NiAs molar ratio

and placed in an alumina crucible that was sealed under $\approx 1/4$ atm high-purity argon in a silica tube. The sealed samples were preheated at 600 °C for 5 h, and then heated to 1300 °C at a rate of 50 °C/h and held there for 15 h for homogenization. Then the furnace was slowly cooled at the rate of 6 °C/h to 1180 °C. The single crystals were separated by decanting the flux with a centrifuge at that temperature. Several 2–4 mm size shiny platelike single crystals were obtained from each growth.

The phase purity and chemical composition of the $\text{Eu}(\text{Co}_{1-x}\text{Ni}_x)_2\text{As}_2$ single crystals were checked using an energy-dispersive x-ray spectroscopy (EDS) chemical analysis attachment to a JEOL scanning-electron microscope (SEM). SEM scans were taken on cleaved surfaces of the crystals which verified the single-phase nature of the crystals. The compositions of each side of a platelike crystal were measured at six or seven positions on each face, and the results were averaged and revealed good homogeneity in each crystal. The results of the composition analyses are given in Table I below. The same crystals were utilized to perform the physical-property measurements.

Single-crystal x-ray diffraction (SCXRD) measurements were performed at room temperature on a Bruker D8 Venture diffractometer operating at a tube voltage of 50 kV and a current of 1 mA equipped with a Photon 100 CMOS detector, a flat graphite monochromator and a Mo $\text{K}\alpha$ $I\mu\text{S}$ microfocus source ($\lambda = 0.71073$ Å). The preliminary quality testing was performed on a set of 32 frames. The raw frame data were collected using the Bruker APEX3 software package [47]. The frames were integrated with the Bruker SAINT program [48] using a narrow-frame algorithm integration and the data were corrected for absorption effects using the multi-scan method (SADABS) [49] within the APEX3 package. The atomic positions were refined assuming partial occupancy of the Ni/Co sites and complete occupancy of the Eu and As sites. Since simultaneous refinement of the fraction of Ni/Co and total occupation of the position is not possible by means of SCXRD, only the total occupancies were refined based on the Ni/Co ratio taken from the EDS data. The atomic displacement parameters were refined anisotropically. Initial models of the crystal structures were first obtained with the program SHELXT-2014 [50] and refined using the program SHELXL-2014 [51] within the APEX3 software package.

A polycrystalline sample of $\text{EuCo}_{2-y}\text{As}_2$ was obtained for ^{151}Eu Mössbauer measurements by crushing several $\text{EuCo}_{2-y}\text{As}_2$ crystals grown in Sn flux; the growth and properties of these crystals are well documented in Ref. [41]. Polycrystalline samples of $\text{Eu}(\text{Co}_{1-x}\text{Ni}_x)_2\text{As}_2$ with $x = 0.2$ and 0.65 for the Mössbauer measurements were synthesized by solid-state reaction using high-purity Eu (Ames Laboratory), and Co (99.998%), Ni (99.999%), and As (99.99999%) from Alfa Aesar. Stoichiometric mixtures of these elements were pelletized and placed in alumina crucibles that were sealed inside evacuated silica tubes. The samples were heated to 900 °C at a

rate of 50 °C/h, held there for 24 h, and then cooled to room temperature at a rate of 50 °C/h. The samples were then thoroughly ground, pelletized, and again sealed in evacuated quartz tubes. The samples were finally sintered at 900 °C for 72 h followed by cooling to room temperature with a 100 °C/h temperature ramping rate. Room-temperature powder XRD measurements were carried out using a Rigaku Geigerflex x-ray diffractometer with $\text{Cu-K}\alpha$ radiation. Structural analyses were performed by Rietveld refinement using the Fullprof software package [52].

Magnetization data were obtained using a Quantum Design, Inc., SQUID-based magnetic-properties measurement system (MPMS) in magnetic fields up to 5.5 T, where 1 T $\equiv 10^4$ Oe, and using the vibrating-sample magnetometer (VSM) option in a Quantum Design, Inc., physical-properties measurement system (PPMS) in magnetic fields up to 14 T. The magnetic moment output of these instruments is expressed in Gaussian cgs electromagnetic units (emu), where 1 emu = 1 G cm³ and 1 G = 1 Oe. The heat capacity $C_p(H, T)$ was measured with a relaxation technique using a PPMS. The $\rho(H, T)$ measurements were performed using a standard four-probe ac technique using the ac-transport option of the PPMS with the current in the *ab* plane. Annealed platinum wire (25 μm diameter) electrical leads were attached to the crystals using silver epoxy.

The ^{151}Eu Mössbauer spectroscopy measurements were carried out using a 4 GBq $^{151}\text{SmF}_3$ source, driven in sine mode and calibrated using a standard $^{57}\text{CoRh}/\alpha\text{-Fe}$ foil. Isomer shifts are quoted relative to EuF_3 at ambient temperature. The sample was cooled in a vibration-isolated closed-cycle helium refrigerator with the sample in helium exchange gas. Where line broadening was not observed (typically at the lowest temperatures and again well above the magnetic transitions) the spectra were fitted to a sum of Lorentzian lines with the positions and intensities derived from a full solution to the nuclear Hamiltonian [53]. The tetragonal $4/mmm$ point symmetry of the Eu site in these materials puts significant constraints on the form of the electric field gradient (efg) tensor, requiring it to be axially symmetric, with the principal component (usually denoted V_{zz}) directed along the crystallographic *c* axis. These features of the efg mean that we are not sensitive to rotations of the moments around the *c* axis, only canting of the moments away from the *c* axis. For example, the incommensurate coplanar *c*-axis helical magnetic structure reported for EuCo_2As_2 [40] has all of the moments perpendicular to the *c* axis with rotations within the *ab*-plane as we move along the *c* axis. This yields a single effective environment for the europium atoms in the ^{151}Eu Mössbauer spectrum, so a sharp single-component spectrum is observed.

TABLE I: Crystallographic data for $\text{Eu}(\text{Co}_{1-x}\text{Ni}_x)_{2-y}\text{As}_2$ single crystals ($x = 0.03\text{--}0.93$) at room temperature, including the fractional c -axis position z_{As} of the As site, the tetragonal lattice parameters a and c , the c/a ratio, the unit cell volume V_{cell} containing $Z = 2$ formula units of $\text{Eu}(\text{Co}_{1-x}\text{Ni}_x)_{2-y}\text{As}_2$, and the molar volume V_{M} , where a mole is a mole of formula units. The Co and Ni compositions and total Co/Ni site occupation in the first column were obtained from EDS analyses, whereas the unit cell parameters and fractional z_{As} coordinates were found from single-crystal structural analyses. The present work is denoted by PW. Corresponding data from the literature for $\text{EuCo}_{2-y}\text{As}_2$ and $\text{EuNi}_{2-y}\text{As}_2$ are also shown.

Compound	z_{As}	a (Å)	c (Å)	c/a	V_{cell} (Å ³)	V_{M} (cm ³ /mol)	Ref.
$\text{EuCo}_{1.94(2)}\text{As}_2$	0.3607(1)	3.9478(7)	11.232(2)	2.845(1)	175.05(7)	52.71(2)	[41]
$\text{Eu}(\text{Co}_{0.97(1)}\text{Ni}_{0.03(1)})_{1.92(1)}\text{As}_2$	0.3609(3)	3.964(8)	11.220(2)	2.831(6)	176.3(8)	53.1(2)	PW
$\text{Eu}(\text{Co}_{0.90(1)}\text{Ni}_{0.10(1)})_{1.92(2)}\text{As}_2$	0.3608(2)	3.978(5)	11.07(1)	2.782(7)	175.1(5)	52.7(2)	PW
$\text{Eu}(\text{Co}_{0.80(1)}\text{Ni}_{0.20(1)})_{1.94(2)}\text{As}_2$	0.3613(1)	3.994(3)	10.836(8)	2.713(4)	172.8(3)	52.03(9)	PW
$\text{Eu}(\text{Co}_{0.68(1)}\text{Ni}_{0.32(1)})_{1.94(2)}\text{As}_2$	0.3628(3)	4.027(2)	10.573(5)	2.625(2)	171.5(2)	51.64(6)	PW
$\text{Eu}(\text{Co}_{0.58(1)}\text{Ni}_{0.42(1)})_{1.94(1)}\text{As}_2$	0.36396(4)	4.046(9)	10.462(2)	2.585(1)	171.2(8)	51.5(2)	PW
$\text{Eu}(\text{Co}_{0.46(1)}\text{Ni}_{0.54(1)})_{1.94(2)}\text{As}_2$	0.36424(5)	4.062(2)	10.328(5)	2.543(2)	170.3(2)	51.28(6)	PW
$\text{Eu}(\text{Co}_{0.35(2)}\text{Ni}_{0.65(2)})_{1.94(2)}\text{As}_2$	0.36476(5)	4.079(2)	10.268(5)	2.517(2)	170.9(2)	51.46(6)	PW
$\text{Eu}(\text{Co}_{0.25(2)}\text{Ni}_{0.75(2)})_{1.94(2)}\text{As}_2$	0.36531(5)	4.091(2)	10.217(5)	2.497(2)	171.0(2)	51.49(6)	PW
$\text{Eu}(\text{Co}_{0.18(2)}\text{Ni}_{0.82(2)})_{1.94(2)}\text{As}_2$	0.3657(1)	4.100(1)	10.155(3)	2.477(1)	170.7(1)	51.40(3)	PW
$\text{Eu}(\text{Co}_{0.07(1)}\text{Ni}_{0.93(1)})_{1.94(2)}\text{As}_2$	0.36627(4)	4.099(3)	10.092(9)	2.462(4)	169.5(3)	51.04(9)	PW
$\text{EuNi}_{1.95(1)}\text{As}_2$	0.36653(8)	4.1052(8)	10.027(2)	2.442(1)	168.99(7)	50.88(2)	[46]

III. CRYSTAL STRUCTURES

A. Single Crystals

The chemical compositions and crystallographic data for the Ni-doped $\text{EuCo}_{2-y}\text{As}_2$ single crystals obtained from the single-crystal XRD and EDS measurements at room temperature are presented in Table I. The data confirm that $\text{Eu}(\text{Co}_{1-x}\text{Ni}_x)_2\text{As}_2$ with $x = 0$ to 1 adopt the ThCr_2Si_2 -type body-centered tetragonal structure with space group $I4/mmm$. We also confirm partial occupation of the Co/Ni site from both EDS and single-crystal XRD measurements, similar to $\text{EuCo}_{2-y}\text{As}_2$ [41], with concentrations listed in Table I.

The lattice parameters a and c , the c -axis As position parameter z_{As} , the ratio c/a , and the unit-cell volume $V_{\text{cell}} = a^2c$ are plotted versus x in Fig. 1. The c lattice parameter decreases upon Ni doping, whereas the a lattice parameter strongly increases with x . These behaviors give rise to the strongly nonlinear variation of V_{cell} with x . Furthermore, the c/a ratio smoothly decreases with x , whereas the z_{As} increases with x , suggesting important changes to the electronic properties. This smooth decrease in c/a with x indicates the occurrence of a continuous structural crossover from the ucT structure at $x = 0$ to the cT structure at $x = 1$, similar to $\text{Sr}(\text{Co}_{1-x}\text{Ni}_x)_2\text{As}_2$ [54].

The values of c/a for $x = 0.2$ (2.713) and $x = 0.3$ (2.625) are in the vicinity of the crossover at ≈ 2.67 between the ucT and cT structures [29]. We therefore infer that a structural crossover occurs in $\text{Eu}(\text{Co}_{1-x}\text{Ni}_x)_2\text{As}_2$ at $x \approx 0.2$. In the following sections we study how these structure changes due to elec-

tron doping of $\text{EuCo}_{2-y}\text{As}_2$ correlate with the ground-state properties of the system.

B. Polycrystalline samples

Room-temperature powder XRD patterns of the polycrystalline $\text{Eu}(\text{Co}_{1-x}\text{Ni}_x)_2\text{As}_2$ samples with $x = 0.20$ and 0.65 are shown in Figs. 2(a) and 2(b), respectively. The Rietveld refinements confirm that both samples crystallize in the ThCr_2Si_2 -type crystal structure with space group $I4/mmm$. The lattice parameters are found to be $a = b = 4.0027(2)$ Å and $c = 10.8636(8)$ Å for $x = 0.20$, and $a = b = 4.0806(1)$ Å and $c = 10.3261(4)$ Å for $x = 0.65$, similar to the lattice parameters of the respective single crystals in Table I. The refinements yielded full occupancy of the Co/Ni site to within 1% for both samples.

IV. MAGNETIC SUSCEPTIBILITY MEASUREMENTS

The zero-field-cooled (ZFC) magnetic susceptibilities $\chi(H, T) \equiv M(T)/H$ of $\text{Eu}(\text{Co}_{1-x}\text{Ni}_x)_2\text{As}_2$ single crystals with $x = 0, 0.03, 0.10, 0.20, 0.32, 0.42, 0.54, 0.65, 0.75$, and 0.82 measured in an applied field $H = 0.1$ T aligned along the c axis (χ_c , $H \parallel c$) and in the ab plane (χ_{ab} , $H \parallel ab$) are shown in Fig. 3. The Eu-spin T_{N} values of the crystals are estimated from the temperatures of the maxima of $d(\chi_{ab}T)/dT$ versus T [55] and are listed in Table II. $\text{EuCo}_{1.92}\text{As}_2$ exhibits $T_{\text{N}} = 45.1$ K [Fig. 3(a)] as previously reported [41]. The T_{N} decreases

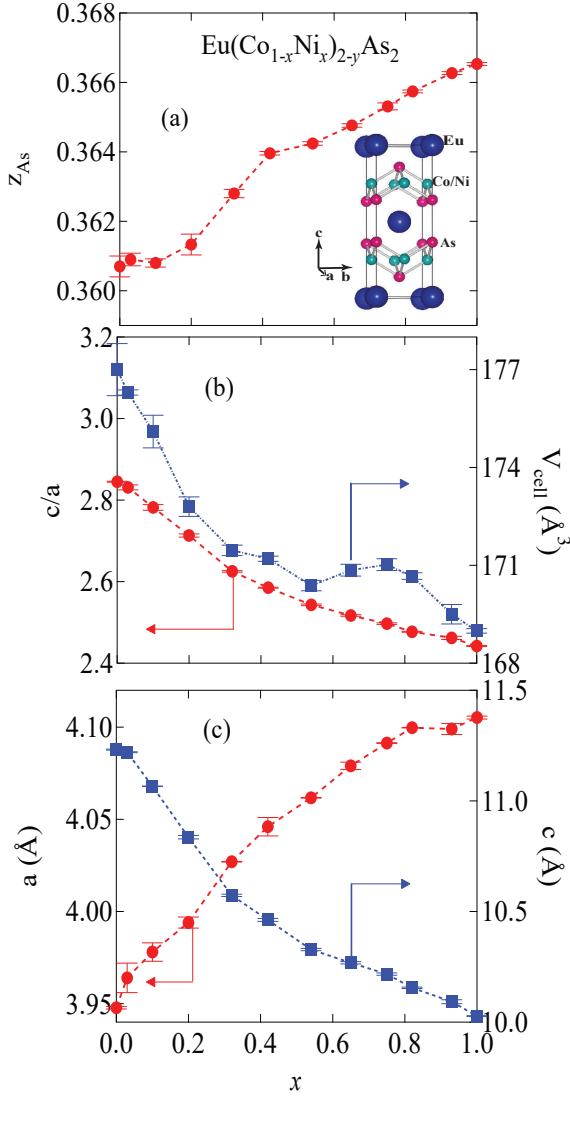


FIG. 1: Crystallographic parameters for $\text{Eu}(\text{Co}_{1-x}\text{Ni}_x)_{2-y}\text{As}_2$ single crystals versus composition x , including (a) the As c -axis parameter z_{As} (b) the c/a ratio and unit-cell volume V_{cell} , and (c) the a and c lattice parameters. The dashed lines are guides to the eye. The inset of (a) shows a unit cell of $\text{Eu}(\text{Co}_{1-x}\text{Ni}_x)_{2-y}\text{As}_2$.

monotonically with increasing Ni doping x and reaches 15 K at $x = 1$, close to the value previously reported for $\text{EuNi}_{1.95}\text{As}_2$ [46]. It is also apparent from Fig. 3 that the magnitude of $\chi_{ab}(T)$ near T_N increases strongly with increasing Ni doping for $x = 0.1, 0.2$, and 0.3 . In particular, the crystal with $x = 0.20$ exhibits the strongest increase in $\chi_{ab}(T_N)$ compared with crystals with compositions on either side. In contrast, for the crystals with $x = 0.42$ – 0.65 , the magnitude of $\chi_c(T)$ is greater than $\chi_{ab}(T)$ near T_N . Furthermore, the system $\text{Eu}(\text{Co}_{1-x}\text{Ni}_x)_{2-y}\text{As}_2$ exhibits an additional transition at $T_{\text{C Co/Ni}}$ for compositions in the range $0.20 \leq x \leq 0.54$ attributed to FM ordering associated with the Co/Ni atoms as shown in

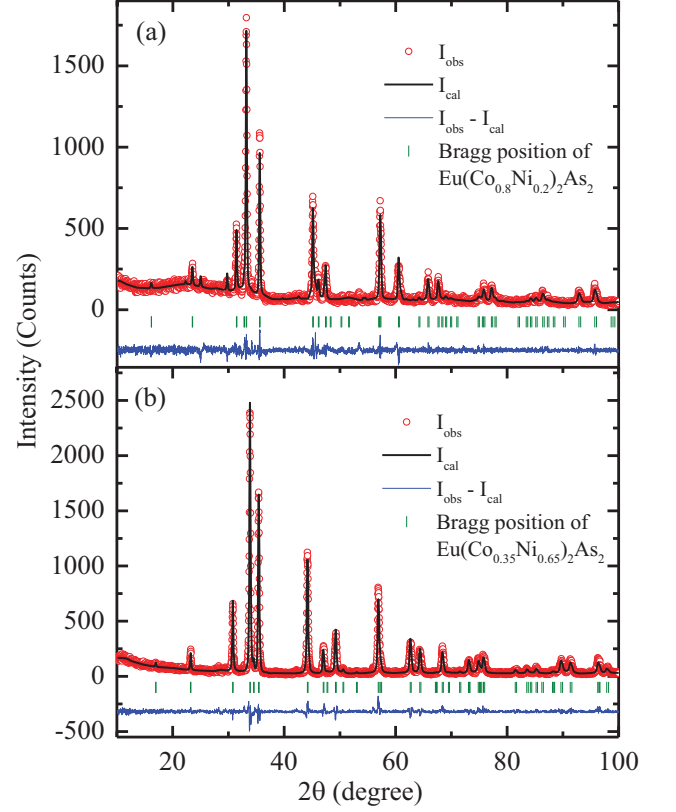


FIG. 2: Room temperature powder XRD patterns along with Rietveld refinement of $\text{Eu}(\text{Co}_{1-x}\text{Ni}_x)_{2-y}\text{As}_2$ polycrystalline compounds for (a) $x = 0.2$ and (b) $x = 0.65$.

TABLE II: Comparison of transition temperatures $T_{\text{N Eu}}$ and $T_{\text{C Co/Ni}}$ of $\text{Eu}(\text{Co}_{1-x}\text{Ni}_x)_{2-y}\text{As}_2$ ($x = 0$ – 1) obtained from magnetic-susceptibility $\chi(T)$ data at an applied field $H = 0.1$ T, and from electrical-resistivity $\rho(T)$ and heat-capacity $C_p(T)$ data in $H = 0$.

x	From $\chi(T)$		From $\rho(T)$		From $C_p(T)$	
	$T_{\text{N Eu}}$ (K)	$T_{\text{C Co/Ni}}$ (K)	$T_{\text{N Eu}}$ (K)	$T_{\text{C Co/Ni}}$ (K)	$T_{\text{N Eu}}$ (K)	$T_{\text{C Co/Ni}}$ (K)
0	45.1(8)		45.0(4)		45.1(2)	
0.03	44(1)		43.9(3)		43.6(2)	
0.1	43(1)		43.1(4)		42.8(1)	
0.2	33(1)	60(2)		58.2(4)	29.8(4)	57.8(4)
0.32	25(1)	66(1)	25.2(3)	66.2(2)	24.2(5)	63.5(6)
0.42	25(1)	58(1)	24.4(3)	58.2(2)	23.9(1)	54.3(2)
0.54	23(1)	40(1)	23.0(8)	39.3(5)	23.0(2)	35.8(5)
0.65	21(1)	25(1)		24.5(8)	20.8(6)	
0.75	19(1)		18.8(2)		17.8(3)	
0.82	16.6(3)		16.5(2)		16.2(4)	
1	14.4(5)		14.2(8)		14.4	

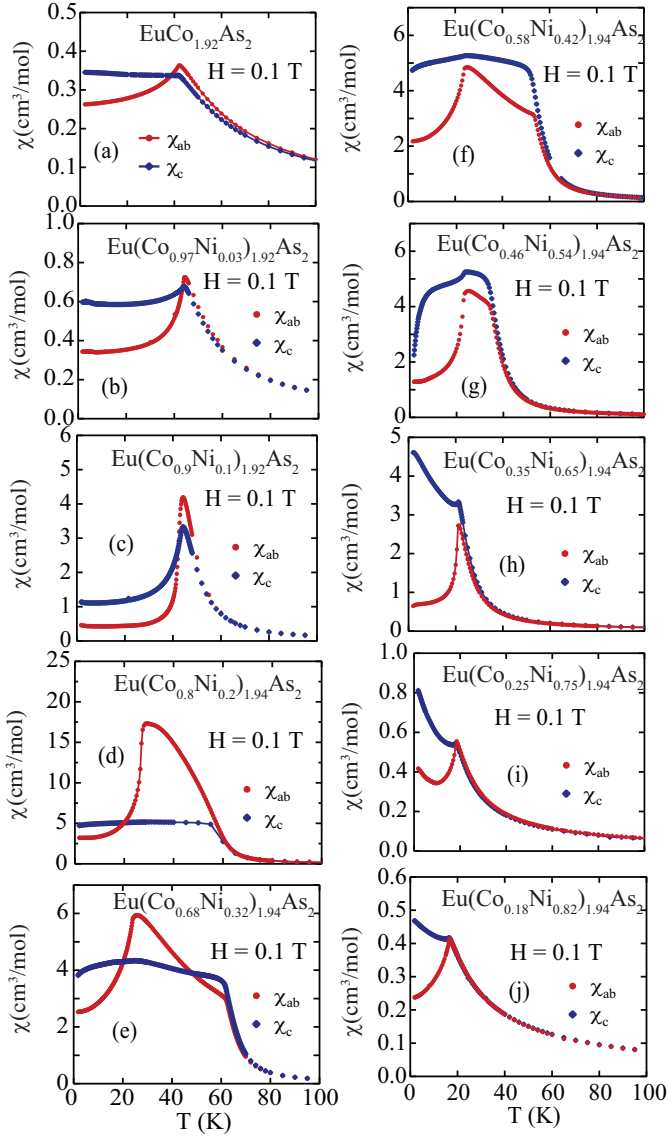


FIG. 3: Zero-field-cooled (ZFC) magnetic susceptibility $\chi \equiv M/H$ of $\text{Eu}(\text{Co}_{1-x}\text{Ni}_x)_{2-y}\text{As}_2$ ($x = 0, 0.03, 0.10, 0.20, 0.32, 0.42, 0.54, 0.65, 0.75$, and 0.82) single crystals as a function of temperature T , from 1.8 to 300 K, measured in magnetic fields $H = 0.1$ T applied in the ab plane (χ_{ab} , $H \parallel ab$) and along the c axis (χ_c , $H \parallel c$). Note the factor of 50 increase in the ordinate scale between $x = 0$ and $x = 0.2$ and the subsequent reduction by the same factor by $x = 0.82$.

Figs. 3(d)–3(g) and listed in Table II.

For the end-point compositions $\text{EuCo}_{2-y}\text{As}_2$ and $\text{EuNi}_{2-y}\text{As}_2$, neutron diffraction [40, 45] and magnetic-susceptibility [46, 54] studies demonstrated that the AFM structure is a planar helix with the Eu ordered moments aligned in the ab plane with the helix axis being the c axis. The data for $x = 0.65$ – 0.82 suggest a c -axis helix magnetic structure as in the end-point compounds whereas the data for $x = 0.03$ and 0.10 suggest the superposition of a c -axis helix and an ab -plane helix where the moments are aligned in an ab - c plane perpendicular to

the ab -plane helix axis. However, the $\chi(T)$ data for intermediate compositions $x = 0.2$ – 0.54 are more complicated because in this composition range two transitions are observed: a likely transition to a c -axis cone structure with a c -axis FM component and a higher-temperature ferromagnetic transition associated with the Co/Ni atoms that is likely of itinerant origin (see below). Coupled with these observations, the scale of the ordinates in Fig. 3 increases by more than an order of magnitude between $x = 0$ and 0.2 , remains larger than for $x = 0$ from $x = 0.32$ to $x = 0.75$, then returns to the scale for $x = 0$ at $x = 1$. In the following two sections we first discuss the helical orderings and then the ferromagnetically ordered component.

A. Helical antiferromagnetic ordering

In this section we analyze the anisotropic $\chi(T)$ data for $x = 0.03, 0.10$, and 0.65 – 0.82 in Fig. 3 in terms of helical ordering. We also include the data and analyses of single-crystal $\chi(T)$ data for the $x = 0$ and 1 end-point compounds [46, 54]. As described in Refs. [35, 36], for a Heisenberg spin system that has a helical AFM structure with the moments aligned in the ab plane of a tetragonal crystal structure, χ_c is independent of T and spin S below T_N whereas χ_{ab} monotonically decreases as the temperature decreases below T_N as shown for $x = 0$ in Fig. 3(a).

When there is anisotropy above T_N , for example due to anisotropic FM fluctuations that appear to be present in the $\text{Eu}(\text{Co}_{1-x}\text{Ni}_x)_{2-y}\text{As}_2$ system, we first take the spherical average of the data above T_N giving $\chi_J(T)$, thus eliminating the effects of anisotropy above T_N . Then we translate the $\chi_{ab}(T \leq T_N)$ and $\chi_c(T \leq T_N)$ data vertically so that they meet the now isotropic PM $\chi_J(T \geq T_N)$ data at T_N . The results of this procedure for the crystals with $x = 0$ [54], 0.03 , 0.10 , and 0.65 – 0.82 are shown in Fig. 4.

Within a one-dimensional J_0 – J_1 – J_2 MFT model for a c -axis Heisenberg helix, one obtains [35, 36]

$$\frac{\chi_{ab}(T \rightarrow 0)}{\chi_{ab}(T_N)} = \frac{1}{2[1 + \cos(kd) + \cos^2(2kd)]}, \quad (1)$$

where kd for a c -axis helix is the turn angle from magnetic-moment layer to layer along the c axis between ferromagnetically aligned moments aligned in the ab plane. A plot of this ratio versus kd is shown in Fig. 5 [35, 36]. It is evident that if the ratio is less than $1/2$, there is only one solution to the turn angle kd . However, for ratios between $1/2$ and 1 , there are two possible solutions. By comparison with neutron diffraction results if available, one can choose the appropriate value for the latter value. If no such additional information is available, one can choose the more likely value from continuity of kd with composition on approaching $x = 0$ or $x = 1$. From the data for $x = 0$ and $x = 1$ in Fig. 4 and a comparison of the two calculated kd values for

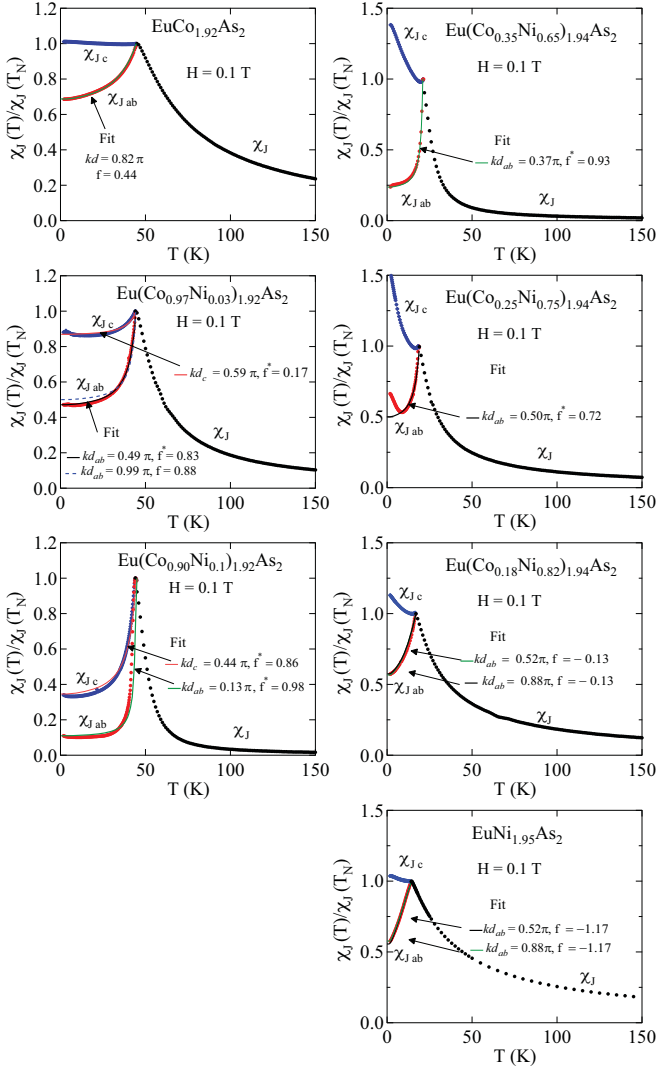


FIG. 4: Anisotropic magnetic susceptibility $\chi(T)$ of $\text{Eu}(\text{Co}_{1-x}\text{Ni}_x)_2\text{As}_2$ crystals with $x = 0$ [54], 0.03, 0.10, 0.65, 0.75, 0.82 from Fig. 3, where the spherical average of the ab -plane and c -axis data were obtained for $T > T_N$, and then the $\chi_{ab}(T)$ and $\chi_c(T)$ data below T_N translated vertically to match the former data at T_N . The values $f = \theta_{\text{p ave}}/T_N$ are measured values, whereas the f^* values are fitted.

each composition with the respective neutron-diffraction data, Eq. (1) gives $kd = 0.85\pi$ rad for $x = 0$ [41] and $kd = 0.88\pi$ rad for $x = 1$ [46], where both values are in good agreement with the respective neutron-diffraction results [40, 45].

Within MFT, for $T \leq T_N$ the perpendicular susceptibility χ_c of a c -axis helical Heisenberg AFM is predicted to be independent of T (and S), in reasonable agreement with the data for $x = 0$ and $x = 1$ in Fig. 4. The normalized T -dependent ratio $\chi_{ab}(T \leq T_N)/\chi(T_N)$ within the J_0 - J_1 - J_2 Heisenberg model is given by [35, 36]

$$\frac{\chi_{ab}(T \leq T_N)}{\chi(T_N)} = \frac{(1 + \tau^* + 2f + 4B^*)(1 - f)/2}{(\tau^* + B^*)(1 + B^*) - (f + B^*)^2}, \quad (2a)$$

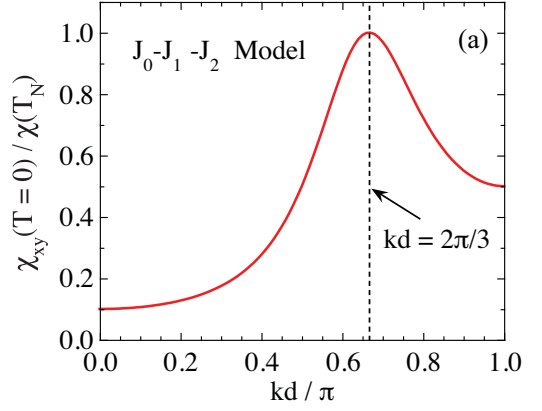


FIG. 5: The ratio $\chi_{xy}(T = 0)/\chi(T_N)$ ($xy = ab$ here) versus the turn angle kd/π between FM-aligned ab -plane layers for a c -axis Heisenberg helix [35, 36]. For $kd = 2\pi/3$, $\chi_{xy} = \chi_z$ ($z = c$ here) is predicted to be independent of both the spin S and T for $T \leq T_N$, as observed [35].

where $f = \theta_{\text{p ave}}/T_N$, $\theta_{\text{p ave}}$ is the spherically averaged Weiss temperature obtained from the Curie-Weiss fit of the $\chi(T)$ data in the paramagnetic state as listed in Table IV below,

$$B^* = 2(1 - f) \cos(kd) [1 + \cos(kd)] - f, \quad (2b)$$

$$t = \frac{T}{T_N}, \quad \tau^*(t) = \frac{(S + 1)t}{3B'_S(y_0)}, \quad y_0 = \frac{3\bar{\mu}_0}{(S + 1)t}, \quad (2c)$$

kd is the turn angle between the magnetic moments in adjacent planes along the helix c axis of ab -plane FM-aligned moment layers, and the ordered moment versus T in $H = 0$ is denoted by μ_0 . The reduced ordered moment $\bar{\mu}_0 = \mu_0/\mu_{\text{sat}}$ with the saturation moment $\mu_{\text{sat}} = gS\mu_B$ is determined by numerically solving the self-consistency equation

$$\bar{\mu}_0 = B_S(y_0), \quad (2d)$$

where $B_S(y)$ is the Brillouin function, and $B'_S(y_0) \equiv [dB_S(y)/dy]|_{y=y_0}$. For $x = 0$ and $x = 1$, the data in Fig. 4 agree well with the MFT prediction for $\chi_{ab}(T \leq T_N)/\chi(T_N)$, following MFT behavior for a c -axis helix with $\mu_{\text{sat}} = 7\mu_B$. For $x = 0$ with $T_N = 45.1$ K, one has $f = 0.44$ and $kd = 0.82\pi$ rad [41], whereas for $x = 1$, $T_N = 14.4$ K, $f = -1.17$, and $kd = 0.88\pi$ rad [46].

The $\chi_\alpha(T < T_N)$ data for $x = 0.03$ and especially for $x = 0.1$ in Fig. 4 are quite interesting, because for these compositions not only does χ_{ab} decrease below T_N , but so does χ_c , an effect that is especially pronounced for $x = 0.1$. This behavior suggests that the AFM structure consists of a superposition of a c -axis helix with the moments aligned in the ab plane and another helix with the helix axis and AFM propagation vector in the ab plane and with the moments aligned in an ab - c plane perpendicular to the in-plane AFM propagation vector, i.e., a

TABLE III: Parameters obtained from fitting the magnetic susceptibility data below T_N of Eu for $\text{Eu}(\text{Co}_{1-x}\text{Ni}_x)_{2-y}\text{As}_2$. Shown are the AFM transition temperature T_N and the Weiss temperature θ_p taken from Table IV below, the observed ratio $f = \theta_p/T_N$, the value f^* obtained from a fit of $\chi_\alpha(T \leq T_N)$ by Eqs. (2), and the turn angle kd between adjacent FM-aligned magnetic layers of the helix model obtained using Eq. (1). For $\chi(T=0)/\chi(T_N) > 1/2$ two values of kd are possible. The notation PW in the last column means the present work.

Compound	field direction	T_N (K)	θ_p (K)	$f = \theta_p/T_N$	f^*	kd (π radian)	kd (degree)	Ref.
$\text{EuCo}_{1.90(1)}\text{As}_2$	$H \parallel ab$	45.1(8)	19.76(9)	0.44		0.82	147	[41]
$\text{Eu}(\text{Co}_{0.97(1)}\text{Ni}_{0.03(1)})_{1.92}\text{As}_2$	$H \parallel ab$	44(1)	38.9(5)	0.88	0.83	0.49	88	PW
	$H \parallel c$		37.30(3)	0.84	0.17	0.59, 0.74	108, 133	PW
$\text{Eu}(\text{Co}_{0.90(1)}\text{Ni}_{0.10(1)})_{1.92}\text{As}_2$	$H \parallel ab$	43(1)	51.2(1)	1.19	0.98	0.13	23	PW
	$H \parallel c$		50.75(6)	1.18	0.86	0.44	79	PW
$\text{Eu}(\text{Co}_{0.35(2)}\text{Ni}_{0.65(2)})_{1.94}\text{As}_2$	$H \parallel ab$	21(1)	18.10(9)	0.86	0.93	0.37	67	PW
$\text{Eu}(\text{Co}_{0.25(1)}\text{Ni}_{0.75(1)})_{1.94}\text{As}_2$	$H \parallel ab$	19(1)	6.74(6)	0.37	0.72	0.50, 0.92	91, 166	PW
$\text{Eu}(\text{Co}_{0.18(1)}\text{Ni}_{0.82(1)})_{1.94}\text{As}_2$	$H \parallel ab$	16.6(3)	-2.3(1)	-0.13		0.52, 0.88	94, 159	PW
$\text{EuNi}_{1.95}\text{As}_2$	$H \parallel ab$	14.4(5)	-15(1)	-1.17		0.88	159	[46]

* fitted parameter

so-called $2q$ structure. Therefore, for $x = 0.03$ and 0.1 we fitted both the χ_{ab} and χ_c data separately by the prediction in Eqs. (2) for the in-plane susceptibility for a helix, and good fits to both data sets were obtained as shown in Fig. 4. A summary of the quantities discussed above is given in Table III.

As discussed in the following section, a FM component to the ordering develops for $0.2 \leq x \leq 0.65$ which contains contributions from both the Eu spins and the Co/Ni sublattice. The occurrence of the FM component for $x = 0.65$ is correlated with the upturn in $\chi_c(T < T_N)$ in Fig. 4 for this composition, but the $\chi_{ab}(T < T_N)$ data in Fig. 4 follow the same behavior as for $x = 0.75-1$, so we include these data in the analysis of the $\chi_{ab}(T \leq T_N)$ data for crystals with compositions in the range $0.65 \leq x \leq 1$.

Figure 6 shows the helical angle kd/π versus x for our crystals for which a helical magnetic structure can be identified from the magnetic susceptibility data. A turn angle $kd/\pi < 1/2$ is indicative of a net ferromagnetic nearest-layer interaction, whereas a value $kd/\pi > 1/2$ indicates a net antiferromagnetic interaction. Therefore the data indicate that at intermediate compositions a net FM interaction develops between the Eu spins in adjacent layers, whereas near the ends of the composition range the net interaction is AFM.

B. Ferromagnetic-ordering component

To further investigate the magnetic behavior, we carried out zero-field-cooled (ZFC) measurements of $\chi(T)$ on warming and field-cooled (FC) measurements of $\chi(T)$ on cooling (FC) versus T in the range 1.8 to 100 K with a small applied field $H = 100$ Oe for the crystals with $x = 0.20, 0.32, 0.42, 0.54$, and 0.65 for both $H \parallel ab$ and $H \parallel c$ which are plotted in Figs. 7(a)–7(e), respec-

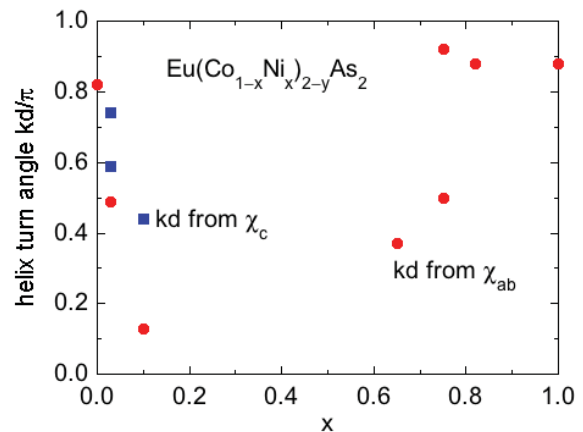


FIG. 6: Helix turn angle(s) versus composition obtained from the ab -plane susceptibility χ_{ab} (filled red circles) and the c -axis susceptibility χ_c (filled blue squares) at temperatures $T < T_N$. For $\chi_\alpha(0)/\chi(T_N) > 1/2$, two values of kd/π are possible according to Fig. 5, indicated by two values of kd/π for the same composition x and for the particular field direction α of χ_α . The large gap between data points at $x = 0.1$ and $x = 0.65$ is present because the Eu magnetic structure between these two compositions is not a simple helix (see text).

tively. The ZFC data were taken after quenching the superconducting magnet to eliminate remanent fields in the magnet. These data show virtually no hysteresis between the ZFC and FC measurements for $H \parallel ab$ but strong hysteresis below the high- T transition for $H \parallel c$. This indicates that there exists a high- T FM transition for $x = 0.2-0.54$ in addition to the AFM ordering of the Eu spin sublattice. Then from Fig. 3, we can assign the low- T transition to an AFM transition involving the Eu spins designated as $T_{N\text{Eu}}$ and the higher- T transitions to FM ordering associated with the Co/Ni atoms

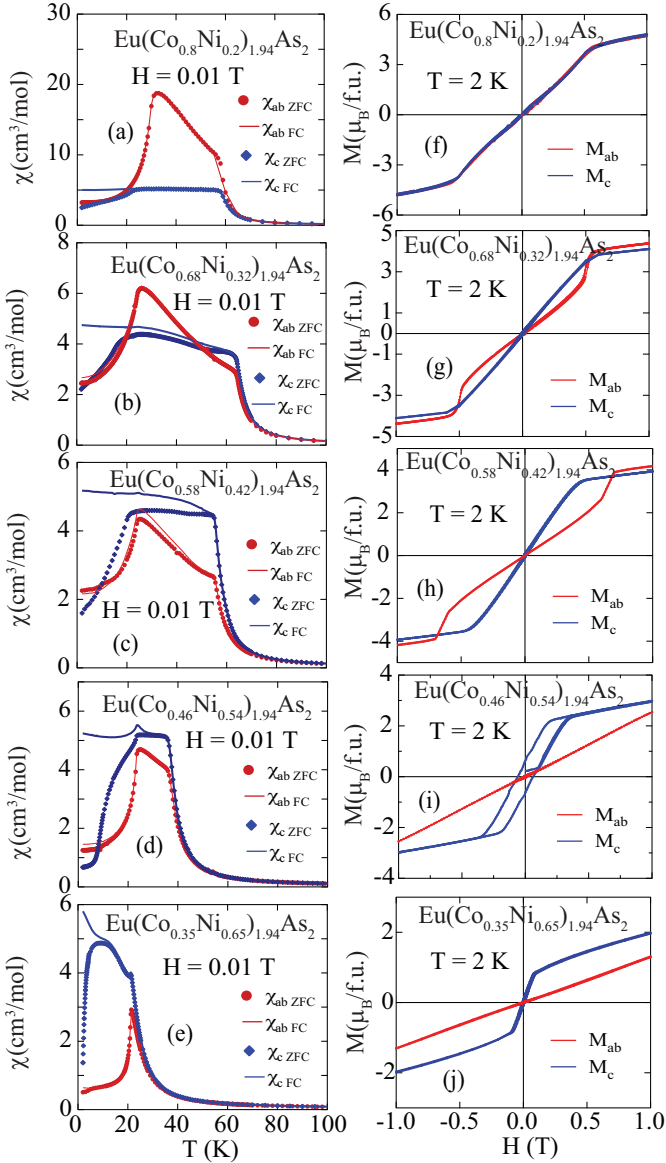


FIG. 7: (a)–(e) Zero-field-cooled (ZFC) and field-cooled (FC) magnetic susceptibility $\chi \equiv M/H$ of $\text{Eu}(\text{Co}_{1-x}\text{Ni}_x)_{2-y}\text{As}_2$ ($x = 0.20, 0.32, 0.42, 0.54$, and 0.65) single crystals as a function of temperature T , from 1.8 to 100 K, measured in magnetic fields $H = 0.01$ T applied in the ab plane (χ_{ab}) and along the c axis (χ_c). (f)–(j) Low-field isothermal magnetization M of $\text{Eu}(\text{Co}_{1-x}\text{Ni}_x)_{2-y}\text{As}_2$ ($x = 0.20, 0.32, 0.42, 0.54$, and 0.65) single crystals as a function of magnetic field H .

at temperatures denoted by $T_{C\text{Co/Ni}}$. This interpretation is strongly supported by the $C_p(T)$ measurements in Sec. VII below. The transition temperatures estimated from the $\chi(T)$ data are listed in Table II, where $T_{N\text{Eu}}$ decreases monotonically upon doping whereas $T_{C\text{Co/Ni}}$ first increases from 60 K for $x = 0.2$ to 66 K for $x = 0.32$, then decreases for $0.32 \leq x \leq 0.65$ and finally disappears for $x > 0.65$.

This interpretation is also supported by low-field $M(H)$ measurements at $T = 2$ K from -1 to $+1$ T as

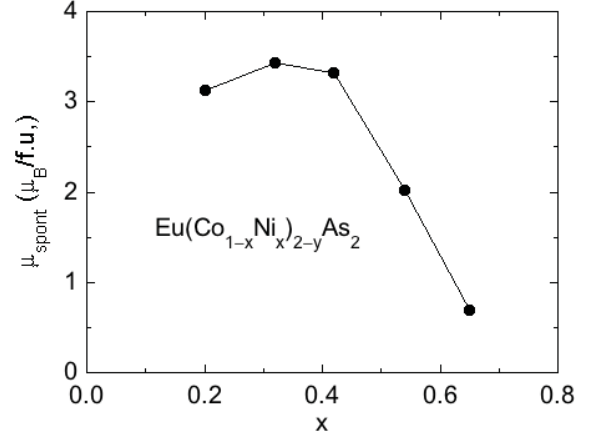


FIG. 8: Spontaneous moment μ_{spont} at $T = 2$ K versus x for $\text{Eu}(\text{Co}_{1-x}\text{Ni}_x)_{2-y}\text{As}_2$ crystals with $x = 0.20, 0.32, 0.42, 0.54$, and 0.65 obtained from the right-hand panels of Fig. 7.

plotted in Figs. 7(f)–7(j) for the same compositions as in Figs. 7(a)–7(e), respectively. An extrapolation of the linear data above the initial field dependence to $H = 0$ gives the spontaneous moment μ_{spont} versus composition plotted in Fig. 8. The variation of μ_{spont} versus x is similar to that of the Co/Ni Curie temperature $T_{C\text{Co/Ni}}$. The large values of μ_{spont} show that the magnetic structure has a large FM component that must arise from the Eu spins. We infer that within the region in which ferromagnetism from the Co/Ni atoms occurs at higher temperatures, the Eu magnetic structure is a c -axis conical structure. In addition, the $M(H)$ data show hysteresis with field for $x = 0.54$ but the hysteresis is very small for the other compositions.

C. Magnetic susceptibility in the paramagnetic state

We now turn our attention to $\chi_\alpha(T)$ ($\alpha = ab$ or c) of the $\text{Eu}(\text{Co}_{1-x}\text{Ni}_x)_{2-y}\text{As}_2$ crystals in the PM region $100 \text{ K} \leq T \leq 300 \text{ K}$. The data are analyzed within the local-moment Heisenberg model in terms of the modified Curie-Weiss law

$$\chi_\alpha(T) = \chi_{0\alpha} + \frac{C_\alpha}{T - \theta_{p\alpha}}, \quad (3)$$

where $\chi_{0\alpha}$ is a T -independent term, the Curie constant per mole of Eu spins is

$$C_\alpha = \frac{N_A g_\alpha^2 S(S+1) \mu_B^2}{3k_B}, \quad (4a)$$

N_A is Avogadro's number, g_α is the possibly anisotropic g factor, and k_B is Boltzmann's constant. The effective moment $\mu_{\text{eff}\alpha} = g_\alpha \sqrt{S(S+1)}$ of a spin in units of μ_B is

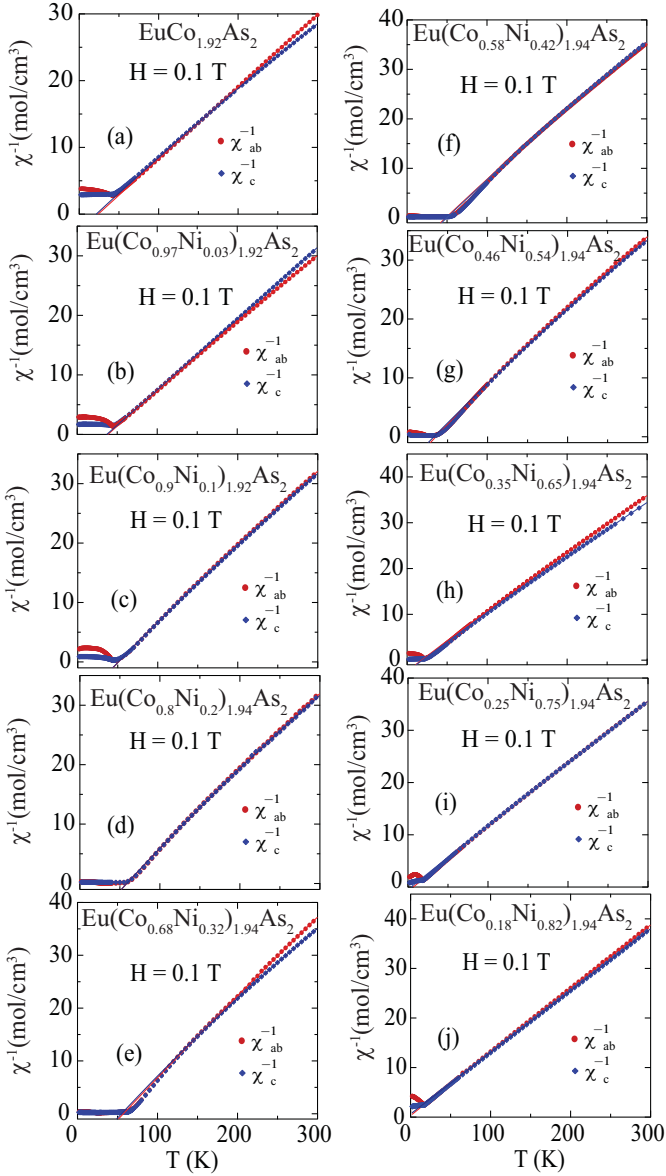


FIG. 9: Inverse susceptibility χ^{-1} of $\text{Eu}(\text{Co}_{1-x}\text{Ni}_x)_{2-y}\text{As}_2$ ($x = 0, 0.03, 0.10, 0.20, 0.32, 0.42, 0.54, 0.65, 0.75$, and 0.82) single crystals as a function of temperature T from 1.8 to 300 K, measured in magnetic fields $H = 0.1$ T applied in the ab plane (χ_{ab}^{-1} , $H \parallel ab$) and along the c axis (χ_c^{-1} , $H \parallel c$).

given by Eq. (4a) as

$$\mu_{\text{eff}\alpha} = \sqrt{\frac{3k_B C_\alpha}{N_A \mu_B^2}} \approx \sqrt{8C_\alpha}, \quad (4b)$$

where C_α is in cgs units of $\text{cm}^3 \text{K}/(\text{mol Eu})$.

Figure 9 shows the inverse susceptibility χ^{-1} with $H = 0.1$ T applied along the c axis (χ_c^{-1}) and in the ab plane (χ_{ab}^{-1}) as a function of T from 1.8 to 300 K. The fits in the PM regime between 100 and 300 K are shown as the solid lines and the fitted parameters are listed in Table IV.

The theoretical values of C_{ave} and $\mu_{\text{eff,ave}}$ for Eu^{+2}

spins with $S = 7/2$ and $g = 2$ are $7.878 \text{ cm}^3 \text{K}/\text{mol Eu}$ and $7.937 \mu_B/\text{Eu}$, respectively. From Table IV, the $\mu_{\text{eff,ave}}$ values significantly decrease gradually from 8.47 to $7.09 \mu_B/\text{Eu}$ for $0 \leq x \leq 0.32$, then increase for $x \geq 0.32$ and finally reach the theoretical value $7.94 \mu_B/\text{Eu}$ for $x = 1$. It is also of note that the $\mu_{\text{eff,ave}}$ values for $0.10 \leq x \leq 0.32$ are much smaller than the theoretical value. The latter observation suggests the possibilities of either an Eu valence increase and/or coexistence of both local moment and itinerant magnetism in $\text{Eu}(\text{Co}_{1-x}\text{Ni}_x)_{2-y}\text{As}_2$. Other types of measurements are required to understand this strange magnetic behavior.

Also apparent in Table IV is a small difference of ≈ 1 K between the Weiss temperatures for fields along the c axis and in the ab plane. This anisotropy may arise from the anisotropic magnetic dipole interactions between the Eu spins [56], from single-ion uniaxial anisotropy [57], and/or from anisotropy in the Ruderman-Kittel-Kasuya-Yosida (RKKY) interactions between Eu spins. The positive $\theta_{\text{p,ave}}$ values for $0 \leq x \leq 0.75$ indicate predominantly FM exchange interactions between the Eu^{+2} spins, whereas for $x = 0.82$ and 1 , the $\theta_{\text{p,ave}}$ values are negative, indicating predominantly AFM exchange interactions.

Figure 10(a) shows plots of $T_{\text{N, Eu}}$, $T_{\text{C Co/Ni}}$, $\theta_{\text{p,ave}}$, and $\mu_{\text{eff,ave}}$ in units of μ_B/Eu from $x = 0$ to 1 . It is informative to plot the ratio $\theta_{\text{p,ave}}/T_{\text{C Co/Ni}}$ versus x and the ratio of $\mu_{\text{eff,ave}}$ to the value $7.94 \mu_B/\text{Eu}$ versus x that the Eu spins would have for $S = 7/2$ and $g = 2$. These ratios are plotted in Fig. 10(b). Several important features are evident from Fig. 10(b). First, relative to the expected value of $7.94 \mu_B/\text{Eu}$ expected for Eu^{+2} with $S = 7/2$ and $g = 2$, μ_{eff} is enhanced for $x = 0$ as previously reported [41]. However, on Ni doping this ratio decreases rapidly and reaches about 89% of the expected value at $x = 0.3$, then reverses course and increases, reaching the expected value of unity at $x = 0.7$ and remaining at that value up to full substitution of Ni for Co at $x = 1$. The deviations of this ratio from unity may reflect the composition-dependent polarization of the Co $3d$ bands by the Eu moments. Alternatively, the negative deviation of this ratio from unity may reflect the presence of an intermediate-valent state for the Eu atoms, where Eu^{+3} does not carry a local moment. However, the latter possibility is ruled out for $x = 0.2$ and 0.65 by the ^{151}Eu Mössbauer measurements in Sec. VI below.

The second important feature of Fig. 10(b) is that the ratio $f = \theta_{\text{p,ave}}/T_{\text{C Co/Ni}}$ is nearly independent of composition with a value close to unity. In a local-moment picture, $f \approx 1$ is only found for a ferromagnet or a material which is nearly ferromagnetic [36]. This result is therefore consistent with the conclusion in Sec. IV B that between $x = 0.2$ and 0.65 the system has a FM component to the ordering which we show from the heat capacity measurements in Sec. VII is associated with the Co/Ni sublattice.

TABLE IV: Listed are the magnetic transition temperatures $T_{\text{N Eu}}$ for $\text{Eu}(\text{Co}_{1-x}\text{Ni}_x)_{2-y}\text{As}_2$, and $T_{\text{C Co, Ni}}$ if present, together with the parameters obtained from modified Curie-Weiss fits of the magnetic susceptibility data between 100 and 300 K, including the T -independent contribution to the susceptibility χ_0 , Curie constant per mole of formula units C_α with the applied field in the $\alpha = ab, c$ directions, and the Weiss temperature $\theta_{\text{p}\alpha}$. Also listed are the effective moments for Eu^{+2} with $S = 7/2$ and $g = 2$ given by $\mu_{\text{eff}\alpha} = \sqrt{8C_\alpha}$ and the angle-averaged effective moment $\mu_{\text{eff ave}} = (2\mu_{\text{eff}ab} + \mu_{\text{eff}c})/3$.

Compound		$T_{\text{N Eu}}, T_{\text{C Co/Ni}}$ (K)	χ_0 ($10^{-3} \frac{\text{cm}^3}{\text{mol}}$)	C_α ($\frac{\text{cm}^3\text{K}}{\text{mol}}$)	$\mu_{\text{eff}\alpha}$ ($\frac{\mu_B}{\text{f.u.}}$)	$\theta_{\text{p}\alpha}$ (K)	$\mu_{\text{eff,ave}}$ ($\frac{\mu_B}{\text{f.u.}}$)	θ_{pave} (K)	Ref.
$\text{EuCo}_{1.90(1)}\text{As}_2^a$	$H \parallel ab$	45.1(8), —	−1.4(2)	8.98(1)	8.476(4)	19.76(9)	8.47(1)	19.07(7)	[41]
	$H \parallel c$		−1.2(1)	8.970(5)	8.471(2)	17.70(5)			
$\text{Eu}(\text{Co}_{0.97(1)}\text{Ni}_{0.03(1)})_{1.92}\text{As}_2$	$H \parallel ab$	44(1), —	1.6(7)	8.27(5)	8.13(2)	38.9(5)	8.16(2)	38.3(3)	PW
	$H \parallel c$		−0.24(1)	8.45(1)	8.221(5)	37.30(3)			
$\text{Eu}(\text{Co}_{0.90(1)}\text{Ni}_{0.10(1)})_{1.92}\text{As}_2$	$H \parallel ab$	43(1), —	2.44(5)	7.15(1)	7.563(5)	51.2(1)	7.58(5)	51.05(8)	PW
	$H \parallel c$		2.33(2)	7.282(7)	7.632(4)	50.75(6)			
$\text{Eu}(\text{Co}_{0.80(1)}\text{Ni}_{0.20(1)})_{1.94}\text{As}_2$	$H \parallel ab$	33(1), 60(2)	1.7(1)	7.25(4)	7.62(2)	54.3(4)	7.47(1)	52.7(3)	PW
	$H \parallel c$		2.35(3)	6.45(1)	7.183 (5)	49.6(1)			
$\text{Eu}(\text{Co}_{0.68(1)}\text{Ni}_{0.32(1)})_{1.94}\text{As}_2$	$H \parallel ab$	25(1), 66(1)	0.8(2)	6.35(7)	7.13(4)	55.3(8)	7.09(2)	55.2(6)	PW
	$H \parallel c$		3.4(4)	6.15(1)	7.01 (2)	55.0(2)			
$\text{Eu}(\text{Co}_{0.58(1)}\text{Ni}_{0.42(1)})_{1.94}\text{As}_2$	$H \parallel ab$	25(1), 58(1)	2.45(3)	6.52(1)	7.22(1)	48.3(1)	7.38(1)	48.58(9)	PW
	$H \parallel c$		1.93(2)	7.424(7)	7.707 (3)	49.15(7)			
$\text{Eu}(\text{Co}_{0.46(1)}\text{Ni}_{0.54(1)})_{1.94}\text{As}_2$	$H \parallel ab$	23(1), 40(1)	2.83(9)	7.07(3)	7.52(1)	33.6(5)	7.55(1)	33.3(4)	PW
	$H \parallel c$		2.86(5)	7.23(2)	7.60(1)	32.9(2)			
$\text{Eu}(\text{Co}_{0.35(2)}\text{Ni}_{0.65(2)})_{1.94}\text{As}_2$	$H \parallel ab$	21(1), 25(1)	1.21(2)	7.50(7)	7.75(3)	18.10(9)	7.79(2)	18.43(9)	PW
	$H \parallel c$		1.55(2)	7.736(8)	7.867(4)	19.1(1)			
$\text{Eu}(\text{Co}_{0.25(1)}\text{Ni}_{0.75(1)})_{1.94}\text{As}_2$	$H \parallel ab$	19(1), —	0.124(1)	7.88(6)	7.940(3)	6.74(6)	7.97(1)	5.76(7)	PW
	$H \parallel c$		0.080(3)	8.09(1)	8.04(5)	3.8(1)			
$\text{Eu}(\text{Co}_{0.18(1)}\text{Ni}_{0.82(1)})_{1.94}\text{As}_2$	$H \parallel ab$	16.6(3), —	0.252(3)	7.72(1)	7.859(5)	−2.3(1)	7.92(1)	−3.2(1)	PW
	$H \parallel c$		−0.196(2)	8.09(1)	8.044(5)	−5.1(2)			
$\text{EuNi}_{1.95}\text{As}_2$	$H \parallel ab$	14.4(5), —	1.01(2)	7.8(1)	7.90(5)	−15(1)	7.95(3)	−15.2(8)	[46]
	$H \parallel c$		1.09(8)	8.13(3)	8.06(1)	−15.6(5)			

^aGrown in Sn flux

V. HIGH-FIELD MAGNETIZATION VERSUS APPLIED MAGNETIC FIELD ISOTHERMS

Isothermal magnetization versus applied magnetic field $M(H)$ isotherms for $\text{Eu}(\text{Co}_{1-x}\text{Ni}_x)_{2-y}\text{As}_2$ ($x = 0, 0.03, 0.10, 0.20, 0.32, 0.42, 0.54, 0.65, 0.75$, and 0.82) measured at $T = 2$ K with $0 \leq H \leq 14$ T applied in the ab plane ($M_{ab}, H \parallel ab$) and along the c axis ($M_c, H \parallel c$) are shown in Fig. 11. The $M_c(H)$ data are nearly linear in field for $x = 0$ and 0.03 as predicted by MFT for a c -axis helix with the field applied along the helix axis [36]. For the crystal with $x = 0.1$, the $M_c(H)$ data exhibit negative curvature and the crystals eventually show a spontaneous magnetization at low field upon doping for $0.2 \leq x \leq 0.65$ signifying a metamagnetic transition at a field H_{mm}^c . The H_{mm}^c and the critical field $H_{c\perp}$ which separates the AFM from the PM phases versus T are taken to be the fields at which dM/dH versus H exhibit a peak or discontinuity as appear in Fig. 12. The estimated values of H_{mm}^c along the c axis are given in Table V. The H_{mm}^c first appears at 0.48 T for $x = 0.2$, then decreases

upon doping and finally disappears for $x > 0.65$. For the crystals with higher Ni doping $x = 0.75$ and 0.82 , the $M_c(H)$ data are again nearly linear in field in Figs. 11(i) and 11(j) as expected for a c -axis helical antiferromagnet. The saturation moment M_{sat} and the critical field $H_{c\perp}$ are given in Table V. The symbol \perp in $H_{c\perp}$ refers to the critical field with H applied parallel to the c axis, i.e., with H applied perpendicular to the zero-field plane of the ordered moments which is the ab plane in this case. The critical field $H_{c\perp}$ initially shifts to lower field with Ni doping $0 \leq x \leq 0.2$ and then shifts to higher field upon Ni doping with $0.32 \leq x \leq 1$. It is notable that the estimated value of M_{sat} at $H = 14$ T is larger with Ni doping than the theoretical value $\mu_{\text{sat}} = gS\mu_B = 7 \mu_B/\text{Eu}$ for $S = 7/2$ and $g = 2$, except for $x = 0.32$ and 0.82 where $\mu_{\text{sat}} = 7 \mu_B/\text{Eu}$.

For $H \parallel ab$, the $M_{ab}(H)$ data in Fig. 11(a) for $x = 0$ show a metamagnetic transition at $H_{\text{mm}1} \approx 3.9$ T and another at $H_{\text{mm}2}^{ab} \approx 4.5$ T which appears to be second order as reported in Ref. [41]. The transition fields $H_{\text{mm}1}^{ab}$ and $H_{\text{mm}2}^{ab}$ and the critical field $H_{c\parallel}$ which separates the AFM from the paramagnetic (PM) phases are taken to

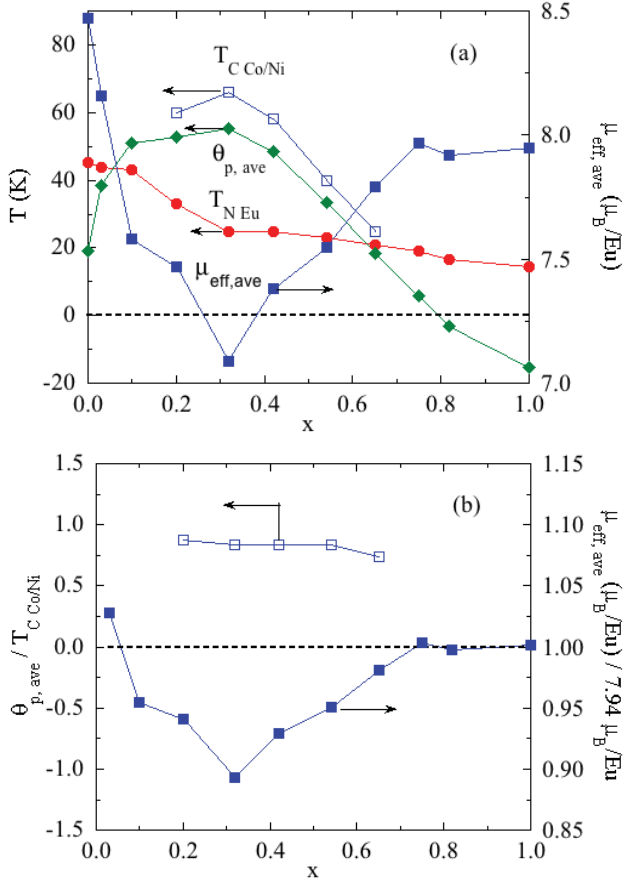


FIG. 10: (a) Néel temperature $T_{\text{N Eu}}$ (filled red circles), spherically averaged Weiss temperature $\theta_{\text{p,ave}}$ (filled green diamonds), average effective moment $\mu_{\text{eff,ave}}$ in μ_B/Eu (filled blue squares), and the second transition temperature $T_{\text{C Co/Ni}}$ (open blue squares) versus x for $\text{Eu}(\text{Co}_{1-x}\text{Ni}_x)_{2-y}\text{As}_2$ crystals. (b) The ratios $f \equiv \theta_{\text{p,ave}}/T_{\text{C Co/Ni}}$ (empty blue squares) and $\mu_{\text{eff,ave}}/(7.94 \mu_B/\text{Eu})$ (filled blue squares) versus x . The value $\mu_{\text{eff}} = 7.94 \mu_B/\text{Eu}$ is the value expected for Eu^{+2} spins with $S = 7/2$ and $g = 2$. The data were obtained from Table IV. The lines are guides to the eye.

be the fields at which dM/dH versus H exhibits a peak or a discontinuity (shown in Fig. 12). The results are given in Table V. One sees that $H_{\text{mm1}}^{\text{ab}}$ disappears with a trace amount of Ni doping whereas $H_{\text{mm2}}^{\text{ab}}$ initially decreases continuously upon Ni doping from 4.5 T at $x = 0$ to 0.5 T at $x = 0.2$ and then increases for $x > 0.2$ and reaches 9.51 T at $x = 1$.

According to Figs. 11(d)–11(f), both $M_{\text{ab}}(H)$ and $M_{\text{c}}(H)$ are almost isotropic for $x = 0.20, 0.32$, and 0.42. As discussed above in Sec. IV B, the $\text{Eu}(\text{Co}_{1-x}\text{Ni}_x)_{2-y}\text{As}_2$ system exhibits two magnetic transitions for $0.2 \leq x \leq 0.65$.

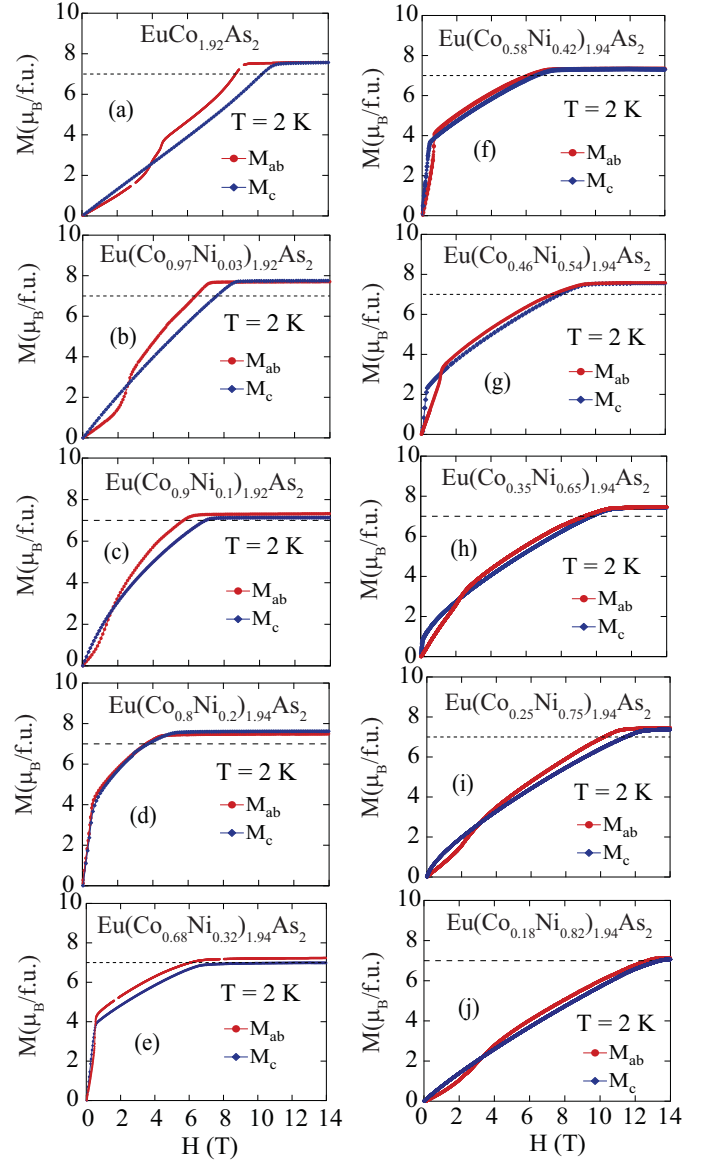


FIG. 11: Isothermal magnetization M of $\text{Eu}(\text{Co}_{1-x}\text{Ni}_x)_{2-y}\text{As}_2$ ($x = 0, 0.03, 0.10, 0.20, 0.32, 0.42, 0.54, 0.65, 0.75$, and 0.82) single crystals as a function of magnetic field H from 0 to 14 T measured at $T = 2$ K with H applied in the ab plane ($M_{\text{ab}}, H \parallel ab$) and along the c axis ($M_{\text{c}}, H \parallel c$). The horizontal dashed lines indicate the magnetization $M = gS\mu_B/\text{Eu} = 7\mu_B/\text{Eu}$ assuming $S = 7/2$ and $g = 2$.

VI. MÖSSBAUER SPECTROSCOPY OF POLYCRYSTALLINE SAMPLES

Magnetic susceptibility data were obtained for the polycrystalline $x = 0.2$ and 0.65 samples used in the Mössbauer experiments. Figures 13(a) and 13(b) (left-hand ordinates) depict $\chi(T)$ of these $\text{Eu}(\text{Co}_{1-x}\text{Ni}_x)_2\text{As}_2$ samples measured in $H = 0.1$ T under zero-field-cooled (ZFC) conditions, respectively. The magnetic transition temperatures obtained from the temperatures of

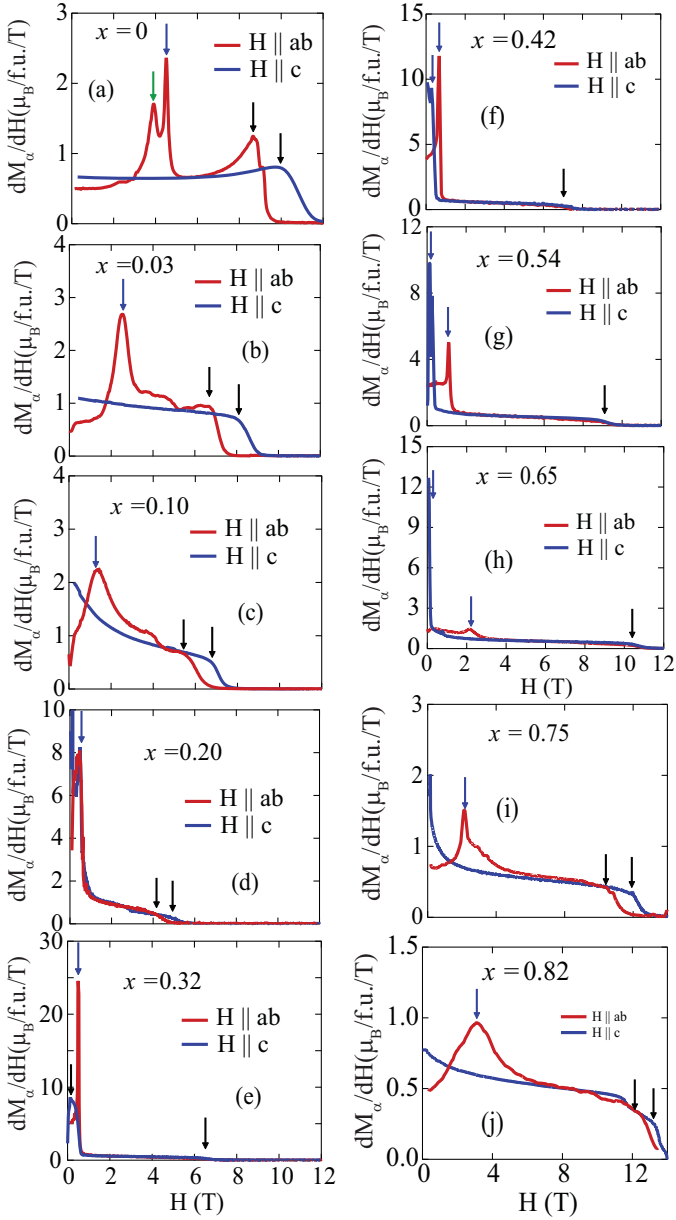


FIG. 12: Derivatives dM_α/dH of the isothermal magnetization $M_\alpha(H)$ of $\text{Eu}(\text{Co}_{1-x}\text{Ni}_x)_{2-y}\text{As}_2$ single crystals ($x = 0, 0.03, 0.10, 0.20, 0.32, 0.42, 0.54, 0.65, 0.75$, and 0.82) from $H = 0$ to 14 T measured at $T = 2$ K with H applied in the ab plane (M_{ab} , $H \parallel ab$) and along the c axis (M_c , $H \parallel c$). The transition fields $H_{\text{mm}1}$ and $H_{\text{mm}2}$ are marked by green and blue arrows, respectively. The critical fields $H_{c\parallel}$ are marked by black arrows.

peaks in $d(\chi T)/dT$ versus T plots (right-hand ordinates) are ~ 54 K and ~ 32 K for $x = 0.2$ and ~ 32 K and ~ 19 K for $x = 0.65$. The higher-temperature troughs in Figs. 13(a) and 13(b) are at the FM ordering temperatures $T_{\text{C Co/Ni}0}$ associated with the Co/Ni atoms and the lower-temperature peaks are at the Néel temperatures $T_{\text{N Eu}}$ of the Eu atoms. The $M(H)$ isotherm at $T = 2$ K for $x = 0.65$ is shown in Fig. 13(c), where the data at low

TABLE V: Metamagnetic fields $H_{\text{mm}1}^{ab}$ and $H_{\text{mm}2}^{ab}$, and the critical fields with the field parallel to the ab plane $H_{c\parallel}$ and parallel to the c axis ($H \parallel c$, $H_{c\perp}$) of $\text{Eu}(\text{Co}_{1-x}\text{Ni}_x)_{2-y}\text{As}_2$ single crystals at $T = 2$ K, determined from the isothermal magnetization $M_\alpha(H)$ data in Figs. 7(f)–7(j), 11, and 12. Also shown are the respective saturation moments μ_{sat} and the spherical average $\mu_{\text{sat,ave}}$, all in units of $\mu_B/\text{f.u.}$

x	$H \parallel ab$				$H \parallel c$			$\mu_{\text{sat,ave}}$ (μ_B)
	$H_{\text{mm}1}^{ab}$ (T)	$H_{\text{mm}2}^{ab}$ (T)	$H_{c\parallel}$ (T)	μ_{sat} (μ_B)	$H_{\text{mm}1}^c$ (T)	$H_{c\perp}$ (T)	μ_{sat} (μ_B)	
0	3.9	4.5	8.79	7.59		9.9	7.57	7.58
0.03		2.6	6.8	7.70		8.02	7.76	7.72
0.10		1.3	5.5	7.32		6.7	7.13	7.25
0.20		0.5	3.6	7.50	0.48	4.6	7.62	7.54
0.32		0.53	6.25	7.23	0.35	6.4	7.01	7.15
0.42		0.77	7.4	7.3	0.28	7.3	7.3	7.3
0.54		1.09	9.2	7.58	0.25	9.3	7.54	7.56
0.65		2.2	10.2	7.44	0.15	10.4	7.44	7.44
0.75		2.1	10.8	7.46		12.1	7.33	7.42
0.82		3.07	12.9	7.19		13.4	7.04	7.14
1	3.15	9.51	> 14			> 14		

fields suggest a FM component to the magnetic ordering and at higher fields the data tend towards saturation of the Eu spins to the expected value $\approx 7 \mu_B/\text{Eu}$.

The ^{151}Eu Mössbauer spectra of $\text{EuCo}_{2-y}\text{As}_2$ shown in Fig. 14 confirm that the europium is fully divalent [isomer shift of $-10.72(2)$ mm/s at 5.4 K] and the sharp lines [HWHM = $1.11(2)$ mm/s] show that the Eu^{+2} moments are in a single magnetic environment with a hyperfine field (B_{hf}) of $26.21(5)$ T. There is a small asymmetry apparent in the spectrum (the four strongest lines increase in intensity going from negative to positive velocity) due to the presence of an electric quadrupole contribution. If we assume that the moments are aligned in the ab plane [40, 41] and are thus perpendicular to V_{zz} ($\theta = 90^\circ$), then we obtain a quadrupole contribution of $-3.2(4)$ mm/s. The contribution is too small for a free fit of both θ and V_{zz} to yield a unique solution.

In all three samples that were studied using ^{151}Eu Mössbauer spectroscopy, we observed significant line broadening at intermediate temperatures. This broadening is too severe to be consistent with a varying canting angle between the c axis and the moments, and its form is inconsistent with the presence of slow paramagnetic relaxation. We conclude that the broadening indicates that time-averaged moments on the europium atoms do not take a single value throughout the sample over the temperature range studied. The form of this broadening is more consistent with the development of a static incommensurate modulated contribution to the magnetic order in which the magnitude of the europium moments varies from site to site within the material. The intermediate-temperature spectra were therefore fitted using a model

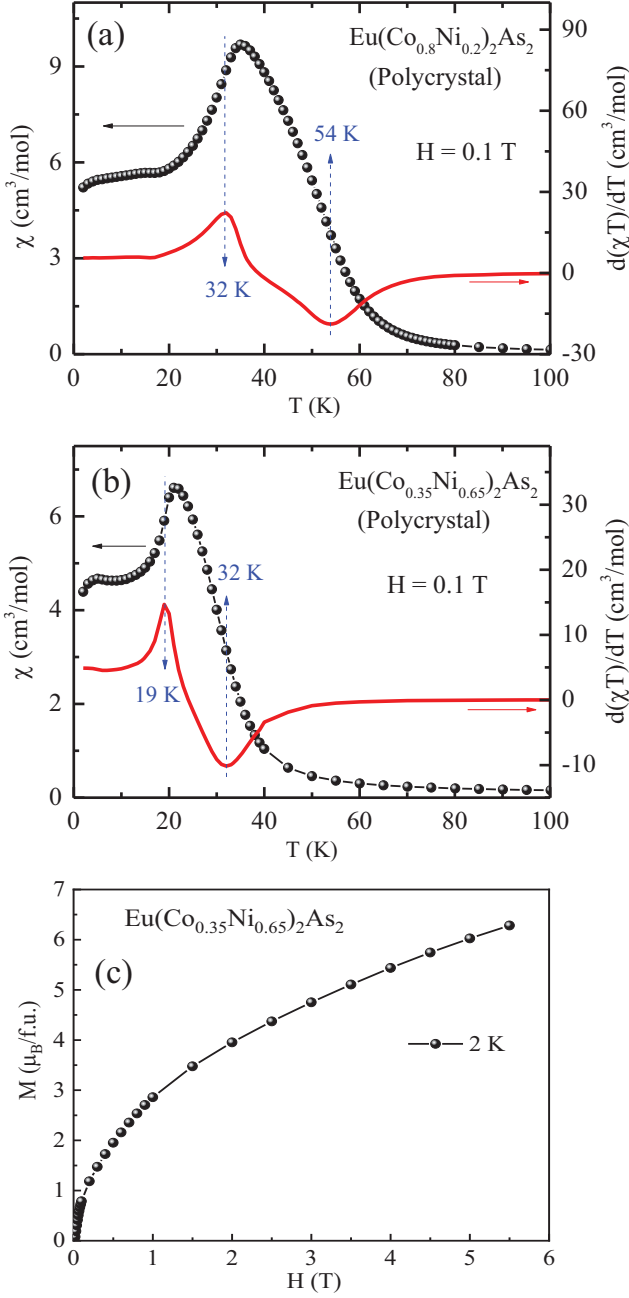


FIG. 13: (Left ordinate) Temperature dependence of the magnetic susceptibility ($\chi = M/H$) in a magnetic field $H = 0.1$ T of Eu(Co_{1-x}Ni_x)₂As₂ polycrystalline samples with (a) $x = 0.20$, and (b) $x = 0.65$. The right ordinate of (a) and (b) is the temperature derivative $d\chi/dT$ versus T obtained from the respective $\chi(T)$ data. (c) Magnetization M versus applied magnetic field H for $x = 0.65$ at $T = 2$ K.

that derives a distribution of hyperfine fields from an (assumed) incommensurate sinusoidally-modulated magnetic structure [58, 59].

If we assume that the moment modulation along the direction of the propagation vector \mathbf{k} can be written in terms of its Fourier components, and further assume that

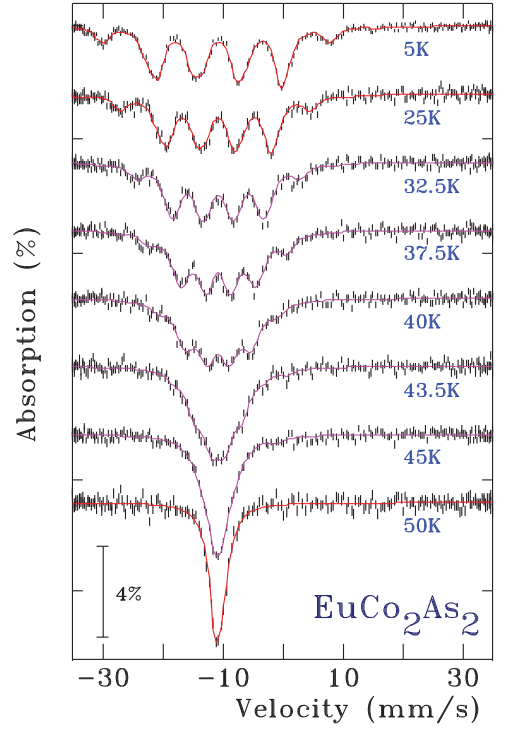


FIG. 14: ¹⁵¹Eu Mössbauer spectra of EuCo_{2-y}As₂ showing the evolution of the spectra with temperature. The solid lines are fits derived from either a full Hamiltonian solution (red lines: $T \leq 30$ K and $T = 50$ K) or from the modulated model (magenta lines: $32.5 \text{ K} \leq T \leq 50 \text{ K}$). See text for details.

the observed hyperfine field is a linear function of the magnitude of the Eu moment at any given site, then the variation of B_{hf} with distance x along the propagation vector \mathbf{k} can be written [58]

$$B_{\text{hf}}(kx) = Bk_0 + \sum_{l=0}^n Bk_{2l+1} \sin[(2l+1)kx], \quad (5)$$

where the Bk_n are the odd Fourier coefficients of the field (moment) modulation. Since $+B_{\text{hf}}$ and $-B_{\text{hf}}$ are indistinguishable, kx only needs to run over half the modulation period, and in this case, a square-wave modulated structure can be modeled either as a sum over a very large number of Fourier coefficients, or by simply using the Bk_0 term with all of the other Bk_n set to zero. We found the fits to be far more stable with the Bk_0 term included rather than using a large set of Bk_n ; however, the two approaches are effectively equivalent. Variations of this model have also been used to fit spectra of EuPdSb [58] and Eu₄PdMg [60].

The sequence for fitting the spectra is as follows. Starting with an initial set of Bk_n , the evolution of B_{hf} along the propagation vector x can be evaluated [a typical example for EuCo_{2-y}As₂ at 40 K is shown in Fig. 15(a)]. From B_{hf} versus kx , a histogram containing the probability $P(B_{\text{hf}})$ versus B_{hf} can be constructed [Fig. 15(b)], and the calculated ¹⁵¹Eu Mössbauer spectrum is then

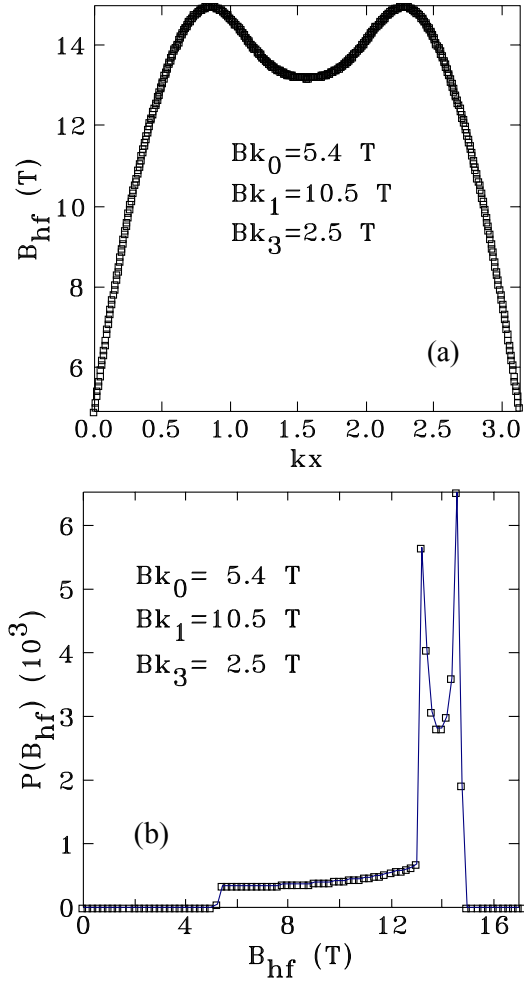


FIG. 15: (a) Variation of the hyperfine field B_{hf} versus kx at $T = 40$ K obtained from the Fourier components of the 40 K data in Fig. 16 and Eq. (5). The third harmonic Bk_3 , not plotted in Fig. 16, is responsible for the dip at $kx = \pi/2$. (b) Unnormalized probability distribution $P(B_{\text{hf}})$ versus B_{hf} .

obtained through a sum of magnetic patterns weighted according to the histogram. A conventional nonlinear least-squares minimization routine is then used to adjust the Bk_n values (and a number of other general parameters including a uniform baseline, overall scale factor, and isomer shift) to minimize χ^2 .

On increasing the temperature, Fig. 16 shows a conventional reduction in the average hyperfine field $B_{\text{avg}}(T)$ where B_{avg} was calculated from the fitted hyperfine field distribution in Eq. (5) using only the positive half of the period. Fitting $B_{\text{avg}}(T)$ by a $S = 7/2$ Brillouin function yields a transition temperature of 45.6(1) K as shown by the black dashed curve in Fig. 16, close to the $T_{\text{N Eu}}$ for $x = 0$ in Table IV. However, closer inspection of the spectra in Fig. 14, particularly the 37.5 K spectrum, reveals a characteristic “settling” towards the center of the pattern consistent with the development of an incommensurate modulation of the magnitude of the moments.

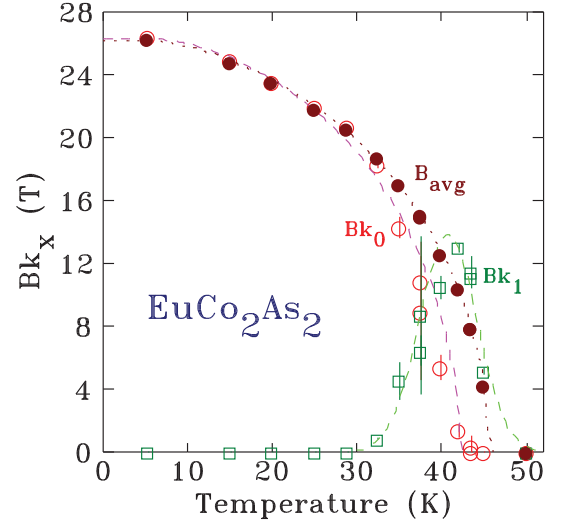


FIG. 16: Temperature dependence of the fitted hyperfine field contributions in EuCo_2As_2 derived from the modulated model. The average hyperfine field (B_{avg}) is plotted as solid round symbols with a dotted line showing a fit (see text) yielding a transition temperature of 45.6(1) K, while the amplitude of the uniform term (Bk_0) is plotted as open round symbols with a dashed line fit giving a transition temperature of 42.0(1) K. The behavior of the first Fourier component (Bk_1) is plotted as open square symbols and shows a peak at 40.8(3) K. The third harmonic $Bk_3(T)$ is not plotted.

The modulated contribution starts to appear by 32.5 K and rapidly comes to dominate the spectrum with increasing temperature. Figure 16 shows that the uniform term (Bk_0) vanishes on heating through 42 K as the first harmonic (Bk_1) peaks. As we will show, this ordering sequence (uniform \rightarrow modulated \rightarrow paramagnetic) is observed on warming in all three of the samples studied here using ^{151}Eu Mössbauer spectroscopy.

From the Fourier components in Fig. 16, one can calculate the hyperfine field B_{hf} seen by the Eu spins versus position along the (unspecified) x axis using Eq. (5). Shown in Fig. 15(a) is a plot of B_{hf} versus kx , where k is the propagation vector of the Eu-spin ordering in the x direction which is presumably the c -axis direction for a c -axis helix. Because the $T = 0$ hyperfine field from Fig. 16 is about 26 T, the modulation of the hyperfine field at 40 K in Fig. 15(a) corresponds to a modulation of the Eu moment of $\approx 0.58(7\mu_B) = 4.0\mu_B$, a rather large modulation. The unnormalized probability distribution $P(B_{\text{hf}})$ versus B_{hf} is plotted in Fig. 15(b). These data were obtained as the inverse of the slope of the plot in Fig. 15(a) versus B_{hf} after binning the data to avoid divergences at the peaks.

It is essential to note that since the magnetic-moment modulation is explicitly assumed to be incommensurate with the crystal lattice, positions along kx in Fig. 15(a) do not correspond in any way to specific positions in the chemical cell. Rather, they represent how B_{hf} , which by assumption is proportional to μ_{Eu} , is sampled by the eu-

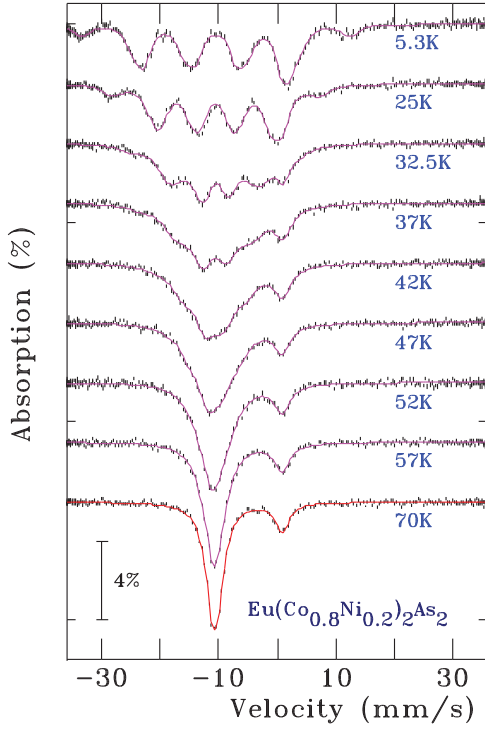


FIG. 17: ^{151}Eu Mössbauer spectra of $\text{Eu}(\text{Co}_{0.8}\text{Ni}_{0.2})_2\text{As}_2$ showing the evolution of the spectra with temperature. The solid lines are fits derived from either a full Hamiltonian solution (red line: $T = 70$ K) or from the modulated model (magenta lines: $T < 70$ K). See text for details. The additional feature near 0 mm/s is due to a nonmagnetic Eu^{+3} impurity, possibly introduced during handling, that accounts for 7.6(4)% of the total spectral area at 5.3 K.

ropium atoms. As the periodicity of the modulation and the crystal cell are not related by a simple rational fraction, neighboring points along the kx axis, in reciprocal space, will be far apart in real space.

Within MFT, if an amplitude-modulated magnetic structure occurs on cooling below T_{NEu} as inferred from Figs. 14–16, the heat-capacity jump on cooling below T_{NEu} is expected to be significantly smaller [61, 62] than the MFT value of 21.4 J/mol spins for $S = 7/2$ [41]. However, for an $\text{EuCo}_{2-y}\text{As}_2$ crystal the measured magnetic contribution $C_{\text{mag}}(T)$ to the heat capacity exhibits a MFT heat capacity jump close to the theoretical value [41].

The ^{151}Eu Mössbauer spectra of $\text{Eu}(\text{Co}_{0.8}\text{Ni}_{0.2})_2\text{As}_2$ shown in Fig. 17 and of $\text{Eu}(\text{Co}_{0.35}\text{Ni}_{0.65})_2\text{As}_2$ shown in Fig. 18 exhibit the same progression as seen for EuCo_2As_2 with one clear difference. There is an additional feature at ~ 0 mm/s that accounts for about 7% of the total area. We attribute this to a nonmagnetic Eu^{+3} impurity, possibly introduced during handling. As this impurity contribution is well defined and consistent in its behavior it is easily included in the analysis without distorting the results.

It is clear from Figs. 19 and 20 that the tempera-

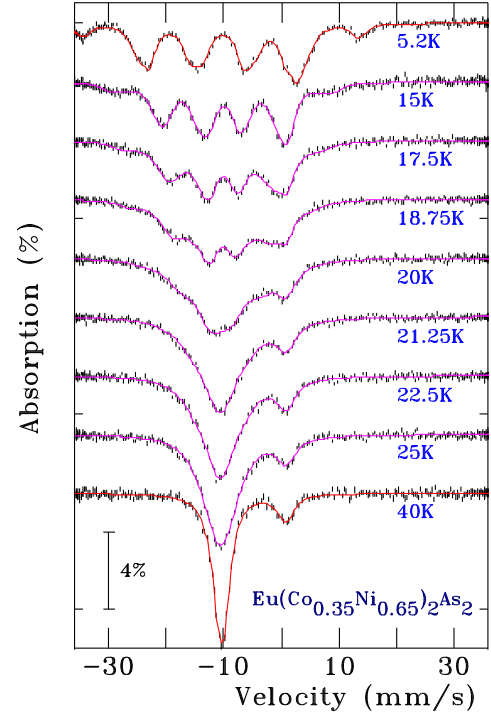


FIG. 18: ^{151}Eu Mössbauer spectra of $\text{Eu}(\text{Co}_{0.35}\text{Ni}_{0.65})_2\text{As}_2$ showing the evolution of the spectra with temperature. The solid lines are fits derived from either a full Hamiltonian solution (red lines: $T = 5.2$ and 40 K) or from the modulated model (magenta lines: $15 \text{ K} \leq T \leq 25 \text{ K}$). See text for details. The additional feature near 0 mm/s is due to a nonmagnetic Eu^{+3} impurity, possibly introduced during handling, that accounts for 7.4(3)% of the total spectral area at 5.2 K.

ture range over which the modulated order is a significant component of the total order is much wider in $\text{Eu}(\text{Co}_{0.8}\text{Ni}_{0.2})_2\text{As}_2$ and $\text{Eu}(\text{Co}_{0.35}\text{Ni}_{0.65})_2\text{As}_2$ than it is in EuCo_2As_2 . For $x = 0.2$ and 65, the uniform term (Bk_0) is lost well before the overall magnetic contribution goes to zero. This leads to the systems exhibiting two distinct transitions. In $\text{Eu}(\text{Co}_{0.8}\text{Ni}_{0.2})_2\text{As}_2$, fitting Bk_0 versus temperature yields $T_c = 36.1(2)$ K while the spectra continue to exhibit magnetic broadening up to ~ 60 K. For $\text{Eu}(\text{Co}_{0.35}\text{Ni}_{0.65})_2\text{As}_2$, the corresponding temperatures are 20.0(1) K and ~ 35 K. These upper temperatures are the same as the FM ordering temperatures associated with the Co/Ni sublattice determined above. By contrast, for $x = 0$, Bk_0 goes to zero at 42 K while the magnetic broadening is gone by 46 K and the two transitions are not well resolved. According to the magnetic susceptibility and magnetization versus field measurements, there is no FM component to the ordering for $x = 0$, so the magnetic broadening up to 46 K may be due to dynamic short-range magnetic ordering above T_{NEu} associated with the Eu spins as revealed in the magnetic contribution $C_{\text{mag}}(T)$ to the heat capacity above T_{NEu} discussed in Sec. VII below.

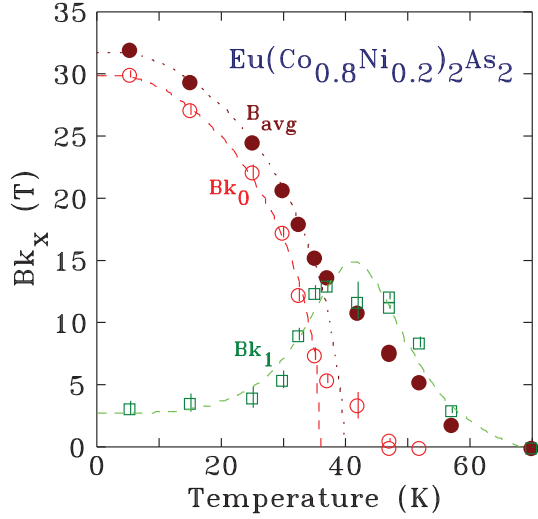


FIG. 19: Temperature dependence of the fitted hyperfine-field contributions in $\text{Eu}(\text{Co}_{0.8}\text{Ni}_{0.2})_2\text{As}_2$ derived from the modulated model. The average hyperfine field (B_{avg}) is plotted as solid round symbols with a dotted line showing a fit (see text) yielding a transition temperature of 40.1(3) K, while the amplitude of the uniform term (Bk_0) is plotted as open circles with a dashed line fit giving a transition temperature of 36.1(2) K. The behavior of the first Fourier component (Bk_1) is plotted as green open squares and shows a broad peak centered at 41.5(6) K. Note: Some magnetic broadening is present at least up to 57 K.

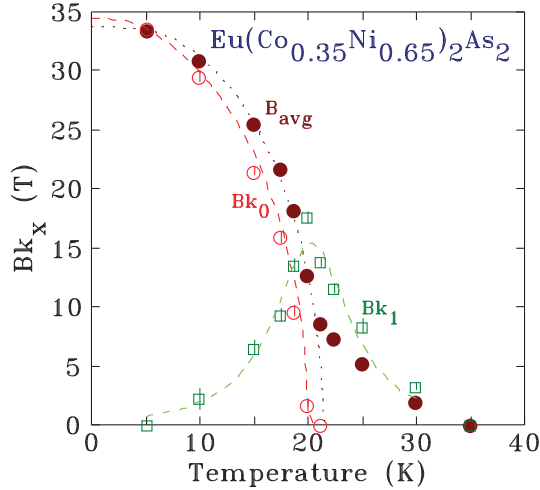


FIG. 20: Temperature dependence of the fitted hyperfine field contributions in $\text{Eu}(\text{Co}_{0.35}\text{Ni}_{0.65})_2\text{As}_2$ derived from the modulated model. The average hyperfine field (B_{avg}) is plotted as solid round symbols with a dotted line showing a fit (see text) yielding a transition temperature of 21.5(1) K, while the amplitude of the uniform term (Bk_0) is plotted as open round symbols with a dashed line fit giving a transition temperature of 20.0(1) K. The behavior of the first Fourier component (Bk_1) is plotted as square symbols and shows a cusp-like peak centered at 20.3(5) K. Note: Some magnetic broadening is present until about 35 K.

x	δ (mm/s)	B_{hf} (T)	$T_c(Bk_0)$ (K)	$T_c(B_{\text{avg}})$ (K)	$T_{\text{pk}}(Bk_1)$ (K)	end (K)
0	-10.72(2)	26.21(5)	42.0(1)	45.6(1)	40.8(3)	46
0.20	-10.53(3)	31.80(8)	36.1(2)	40.1(3)	41.5(6)	60
0.65	-10.30(2)	33.29(7)	20.0(1)	21.5(1)	20.3(5)	32

TABLE VI: Results derived from the analysis of the ^{151}Eu Mössbauer spectra of $\text{Eu}(\text{Co}_{1-x}\text{Ni}_x)_2\text{As}_2$. The isomer shift (δ) and hyperfine field (B_{hf}) are taken from the 5 K spectra. Transition temperatures for fits to the average hyperfine field (B_{avg}) and the uniform term in the Fourier expansion (Bk_0) are given along with the location in the peak of the first harmonic (Bk_1). The final column lists the approximate temperature above which magnetic broadening of the spectrum disappears. For $x = 0.2$ and 0.65 these correspond approximately to the FM transition temperature $T_{\text{C Co/Ni}}$ in Table II associated with the Co/Ni atoms as determined from other measurements.

Discussion

As Mössbauer spectroscopy is fundamentally a short-ranged probe of magnetic order, it provides very little direct information about the detailed nature of the long-range magnetic order in this system. However, some key statements can be made.

There are no significant changes in the isomer shifts of the Eu^{+2} component of the spectra in any of the samples, nor is there any sign of a new Eu^{+3} component (beyond the previously-noted impurity) developing with changing temperature. We therefore conclude that the europium in all three samples remains fully divalent from ~ 5 to ~ 295 K.

At the lowest temperatures in all three samples ($x = 0, 0.20, 0.65$) the europium is in a single magnetic environment (modulo rotations about the c axis, to which the technique is insensitive due to the $4/mmm$ point symmetry of the Eu site).

In all three compositions, the initial ordering of the Eu spins that develops on cooling from the high-temperature paramagnetic state appears to include an incommensurate modulated component in which the magnitudes of the europium moments vary, so that the ^{151}Eu nuclei experience a broad distribution of magnetic environments that can be modeled using a sum of Fourier components. This modulated regime is quite narrow for $x = 0$ but is much broader for $x = 0.20$ and 0.65 .

The magnetic transitions in $\text{EuCo}_{2-y}\text{As}_2$ are only separated by a few degrees (see Table VI) and do not appear to exhibit separate signatures in our other measurements. However, in $\text{Eu}(\text{Co}_{0.8}\text{Ni}_{0.2})_2\text{As}_2$ the two transitions defined by extrapolation of Bk_0 versus T and by the ultimate loss of magnetic splitting in the spec-

trum (“end” column) are about 20 K apart (see Table VI) and are clearly resolved in both $\chi(T)$ and $C_p(T)$. We also see two transitions separated by about 10 K in $\text{Eu}(\text{Co}_{0.35}\text{Ni}_{0.65})_2\text{As}_2$; however, only the lower one is consistently seen by the bulk techniques.

There are two basic possibilities for the nature of the modulated phase. Given that helical order exists at the lowest temperatures, it is possible that in addition to the rotation about the c axis the magnitude of the moments also varies from layer to layer as the upper transition is approached. Alternatively, the long-range order could break down into a short-range correlated state before the long-range order collapses entirely. The former would appear consistent with the behavior of the $x = 0$ and 0.20 samples where the transitions, when resolved, are seen by multiple techniques. The latter form may be more consistent with the behavior of the $x = 0.65$ sample where the upper loss of order is not consistently seen and the decay of $B_{\text{avg}}(T)$ is quite soft, perhaps reflecting a gradual breakdown of magnetic correlations. Only direct measurement by either neutron diffraction or resonant magnetic x-ray diffraction can distinguish these two possibilities.

For $\text{Eu}(\text{Co}_{0.8}\text{Ni}_{0.2})_2\text{As}_2$ (Fig. 19) and $\text{Eu}(\text{Co}_{0.35}\text{Ni}_{0.65})_2\text{As}_2$ (Fig. 20), B_{avg} exhibits a clear tail to high temperatures, well beyond where the extrapolation of the lower temperature behavior would predict that it would go to zero. The observed hyperfine fields are too large to simply be the result of a direct transferred field from the itinerant FM Co/Ni order; however, exchange interactions between the Co/Ni order and the europium moments leading to an effective applied magnetic field supporting the ordering of the europium moments could certainly account for the observed fields. The ^{151}Eu Mössbauer spectra therefore provide further evidence of the Co/Ni order for intermediate nickel doping.

We fitted the neutron-diffraction intensity $I(T)$ of the helical (0 0 2.79) magnetic peak for $\text{EuCo}_{2-y}\text{As}_2$ versus temperature that was presented in Ref. [40]. Because the spin $S = 7/2$ of Eu^{+2} is large, the MFT prediction should be quite accurate. We indeed obtained a good fit to the data by MFT for $S = 7/2$ as shown by the solid blue curve representing the square of the ordered moment versus temperature in Fig. 21, consistent with the good fit of $B_{\text{avg}}(T)$ in Fig. 16, apart from a possible small systematic deviation of the data from the fitted curve in Fig. 21 on approaching $T_{\text{N Eu}}$ from below.

VII. HEAT CAPACITY

Figure 22 shows the heat capacities $C_p(T)$ for $\text{Eu}(\text{Co}_{1-x}\text{Ni}_x)_2\text{As}_2$ single crystals with compositions $x = 0, 0.03, 0.1, 0.2, 0.32, 0.42, 0.54, 0.65, 0.75$, and 0.82, and for the nonmagnetic reference compound BaCo_2As_2 [41] measured in the temperature range from 1.8 to 300 K in zero applied magnetic field. For each com-

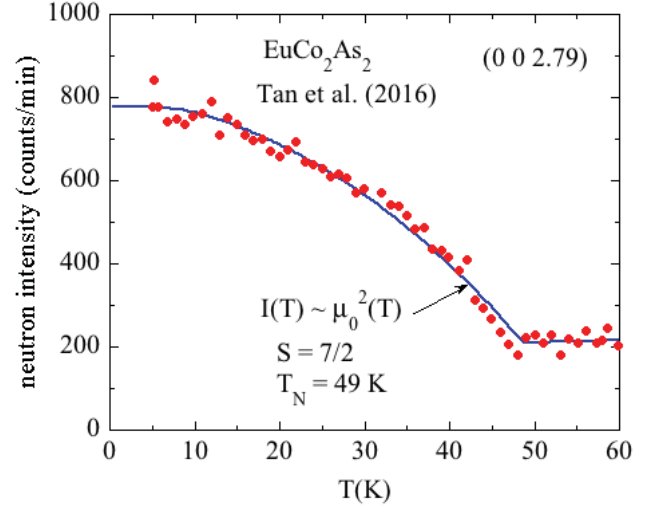


FIG. 21: Neutron intensity $I(T)$ of the helical (0 0 2.79) magnetic peak of $\text{EuCo}_{2-y}\text{As}_2$ reported in Ref. [40] (filled red circles). Our least-squares fit by molecular-field theory for spin $S = 7/2$ [see Eq. (2d)] is shown by the solid blue curve.

position, the $C_p(T = 300 \text{ K})$ of $\text{Eu}(\text{Co}_{1-x}\text{Ni}_x)_2\text{As}_2$ attains a value of $\approx 123.2 \text{ J/mol K}$ which is close to the classical Dulong-Petit high- T limit $C_V = 3nR = 123.2 \text{ J/mol K}$, where $n = 4.94$ is the number of atoms per formula unit and R is the molar gas constant.

The insets in Fig. 22 show plots of C_p/T versus T^2 from 1.8 to 5 K for each crystal. The purpose of these plots is to show that the low-temperature data cannot be fitted by the conventional expression $C_p(T)/T = \gamma + \beta T^2$, where γ is the Sommerfeld coefficient associated with the conduction electrons and β is the coefficient of the T^3 lattice term.

The C_p/T versus T data for the $\text{Eu}(\text{Co}_{1-x}\text{Ni}_x)_2\text{As}_2$ crystals in the temperature range from 1.8 to 10 K are plotted in Figure 23. One sees that each crystal shows approximately linear behavior over a certain T range; for example, for $x = 0$ to 0.32 this range is from 2 to 6 K, whereas for $x \geq 0.54$ the range is below 4 K, which means that C_p has an approximately T^2 contribution over the respective T range. This behavior may arise from the temperature-dependent heat capacity of AFM spin waves.

The $C_p(T)$ data for $\text{Eu}(\text{Co}_{1-x}\text{Ni}_x)_2\text{As}_2$ in the PM regime $100 \text{ K} \leq T \leq 300 \text{ K}$ are analyzed using the sum of an electronic γT term and the lattice term given by the Debye model according to

$$C_p(T) = \gamma T + nC_{\text{V Debye}}(T), \quad (6a)$$

where γ is again the Sommerfeld electronic heat capacity coefficient, $C_{\text{V Debye}}(T)$ is the Debye lattice heat capacity given by

$$C_{\text{V Debye}}(T) = 9R \left(\frac{T}{\Theta_D} \right)^3 \int_0^{\Theta_D/T} \frac{x^4 dx}{(e^x - 1)^2} dx, \quad (6b)$$

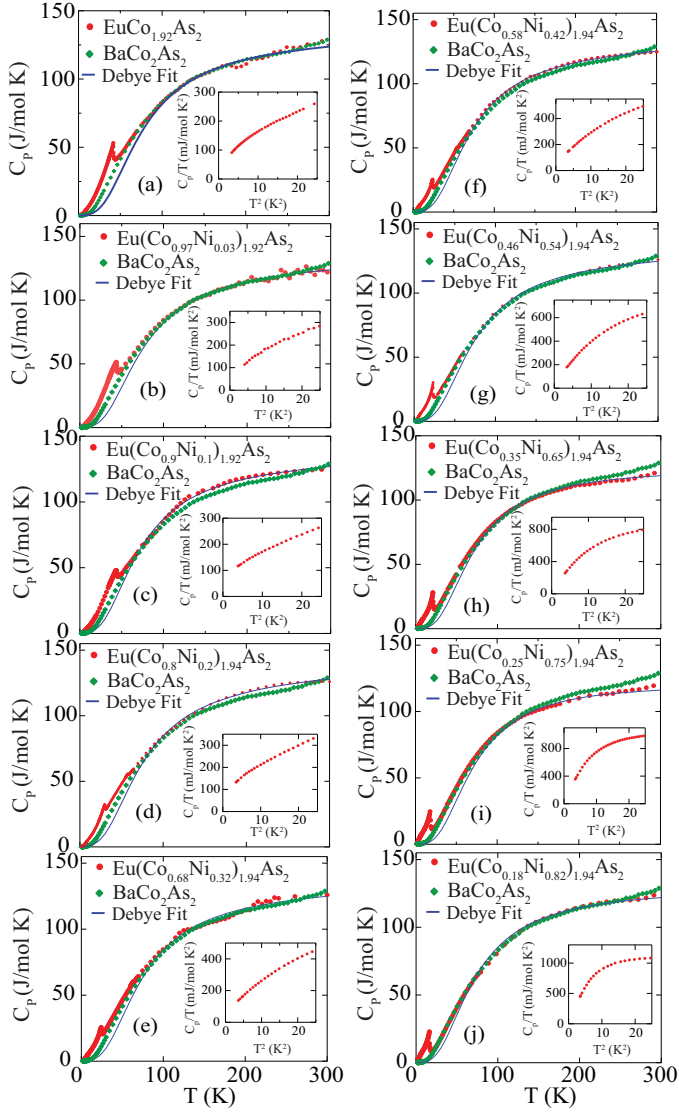


FIG. 22: The temperature T dependence of the heat capacity C_p for $\text{Eu}(\text{Co}_{1-x}\text{Ni}_x)_{2-y}\text{As}_2$ with $x = 0, 0.03, 0.10, 0.20, 0.32, 0.42, 0.54, 0.65, 0.75$, and 0.82 and BaCo_2As_2 single crystals in $H = 0$ T. The solid black curves are fits of the data between 70 and 300 K by the Debye lattice heat capacity model in Eqs. (6). Insets: Expanded plots of $C_p(T)/T$ vs T^2 from 1.8 to 5 K.

and $n = 4.94$ is again the number of atoms per formula unit. The black solid curves in Fig. 22 represent the fits of the $C_p(T)$ data for $100 \text{ K} \leq T \leq 300 \text{ K}$ by Eqs. (6) obtained using the accurate analytic Padé approximant function for $C_{V\text{Debye}}$ versus T/Θ_D given in Ref. [63]. The fitted values of γ and Θ_D for $\text{Eu}(\text{Co}_{1-x}\text{Ni}_x)_{2-y}\text{As}_2$ are listed in Table VII.

The density of degenerate conduction carrier states at the Fermi energy E_F for both spin directions $\mathcal{D}_\gamma(E_F)$ is obtained from γ according to

$$\mathcal{D}_\gamma(E_F) = \frac{3\gamma}{\pi^2 k_B^2}, \quad (7a)$$

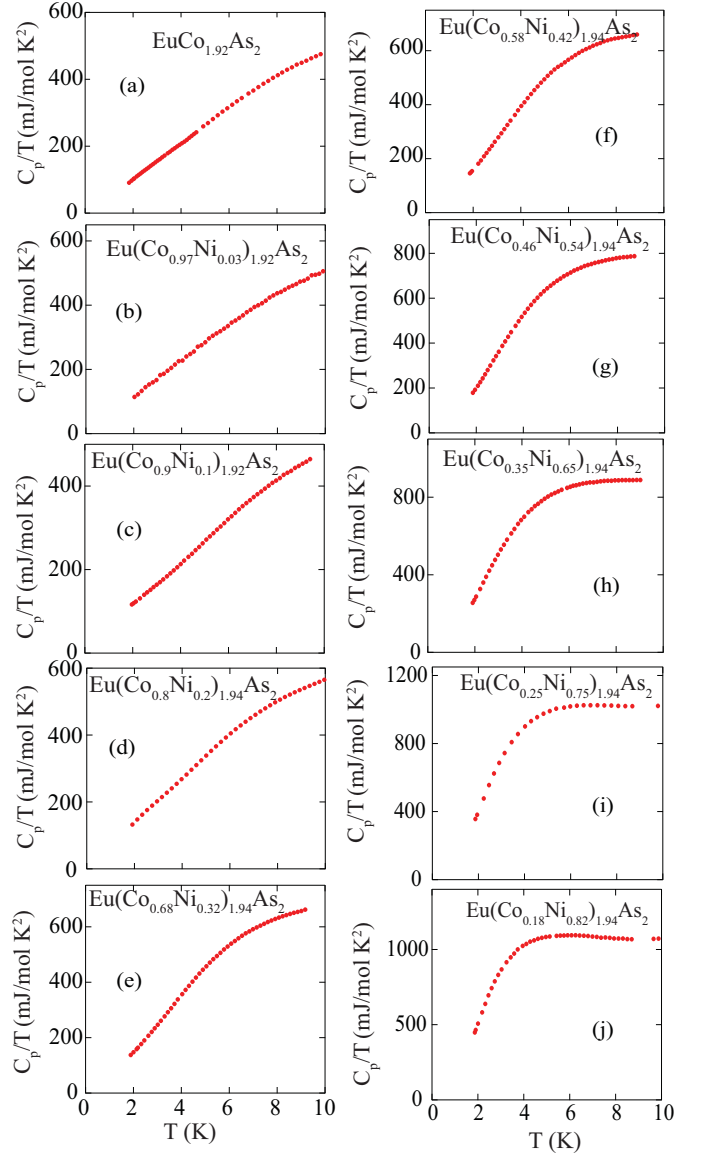


FIG. 23: Heat capacity C_p/T vs T at zero field from 1.8 to 10 K for each $\text{Eu}(\text{Co}_{1-x}\text{Ni}_x)_{2-y}\text{As}_2$ crystal ($x = 0, 0.03, 0.10, 0.20, 0.32, 0.42, 0.54, 0.65, 0.75$, and 0.82).

which gives

$$\mathcal{D}_\gamma(E_F) \left[\frac{\text{states}}{\text{eV f.u.}} \right] = \frac{1}{2.359} \gamma \left[\frac{\text{mJ}}{\text{mol K}^2} \right], \quad (7b)$$

where “mol” refers to a mole of formula units (f.u.). The $\mathcal{D}_\gamma(E_F)$ values calculated for our $\text{Eu}(\text{Co}_{1-x}\text{Ni}_x)_{2-y}\text{As}_2$ crystals from their γ values using Eq. (7b) are listed in Table VII, where the fitted values are close to each other for $x = 0$ to 0.82 .

The magnetic contribution $C_{\text{mag}}(T)$ to $C_p(T)$ of $\text{Eu}(\text{Co}_{1-x}\text{Ni}_x)_{2-y}\text{As}_2$ obtained after subtracting the lattice contribution, taken to be $C_p(T)$ of BaCo_2As_2 [41], is shown in Fig. 24. Within MFT the discontinuity in C_{mag}

TABLE VII: The parameters γ , θ_D and density of states at the Fermi energy $\mathcal{D}_\gamma(E_F)$ obtained from fits to the heat capacity by Eqs. (6) in the temperature range $100 \text{ K} \leq T \leq 300 \text{ K}$.

x	γ (mJ/mol K ²)	θ_D (K)	$\mathcal{D}_\gamma(E_F)$ (states/eV f.u)
0	15(2)	308(3)	6.3(8)
0.03	18(2)	310(3)	7.6(8)
0.1	25(1)	286(2)	10.7(4)
0.2	33(1)	306(1)	13.9(4)
0.32	25(3)	313(5)	11(1)
0.42	23(1)	298(1)	9.7(4)
0.54	23(2)	311(4)	9.7(8)
0.65	23(2)	294(2)	9.7(8)
0.75	22(1)	298(2)	9.3(4)
0.82	21.3(8)	303(2)	9.0(3)

at $T = T_N$ is given by [36]

$$\Delta C_{\text{mag}} = R \frac{5S(1+S)}{1+2S+2S^2} = 20.14 \text{ J/mol K}, \quad (8)$$

where the second equality is calculated for $S = 7/2$. The experimental heat capacity jump for $x = 0$ in Fig. 24(a) at $T_N = 45 \text{ K}$ is $\approx 21.74 \text{ J/mol K}$, somewhat larger than the theoretical prediction of MFT. With doping, the value of ΔC_{mag} decreases to values smaller than the theoretical prediction up to $x = 0.42$, and then increases again. The $C_{\text{mag}}(T)$ is nonzero for $T_N < T \leq 40 \text{ K}$, indicating the presence of dynamic short-range AFM ordering of the Eu spins above $T_{N\text{Eu}}$, thus accounting at least in part for the decrease in ΔC_{mag} from the theoretical value.

From Fig. 24, we find two magnetic transition peaks for $x = 0.2, 0.32, 0.42$, and 0.54 , consistent with the above studies. It is clear that the magnetic ordering of the Eu spins for all compositions is associated with the λ -type anomaly that decreases monotonically from a temperature $T_{N\text{Eu}} = 45.1(2) \text{ K}$ to $16.2(4) \text{ K}$ at $x = 0.84$, as listed above in Table II. We therefore ascribe the upper transition temperature manifested by a step discontinuity in $C_{\text{mag}}(T)$ in Fig. 24 to magnetic ordering of the Co/Ni atoms, which from the above magnetic measurements is FM. Therefore, the latter transition temperatures are denoted by $T_{C\text{Co/Ni}}$ in Table II.

The magnetic entropy is calculated from the $C_{\text{mag}}(T)$ data for $\text{Eu}(\text{Co}_{1-x}\text{Ni}_x)_{2-y}\text{As}_2$ in Fig. 24 using

$$S_{\text{mag}}(T) = \int_0^T \frac{C_{\text{mag}}(T')}{T'} dT', \quad (9)$$

and the results are shown in Fig. 24 (right-hand ordinates). The theoretical high- T limit is $S_{\text{mag}}(T) = R \ln(2S+1) = 17.29 \text{ J/mol K}$ for $S = 7/2$. The entropy reaches almost 90% of $R \ln(8)$ at $T_{N\text{Eu}}$. The high- T limit of the data is slightly different from the theoretical

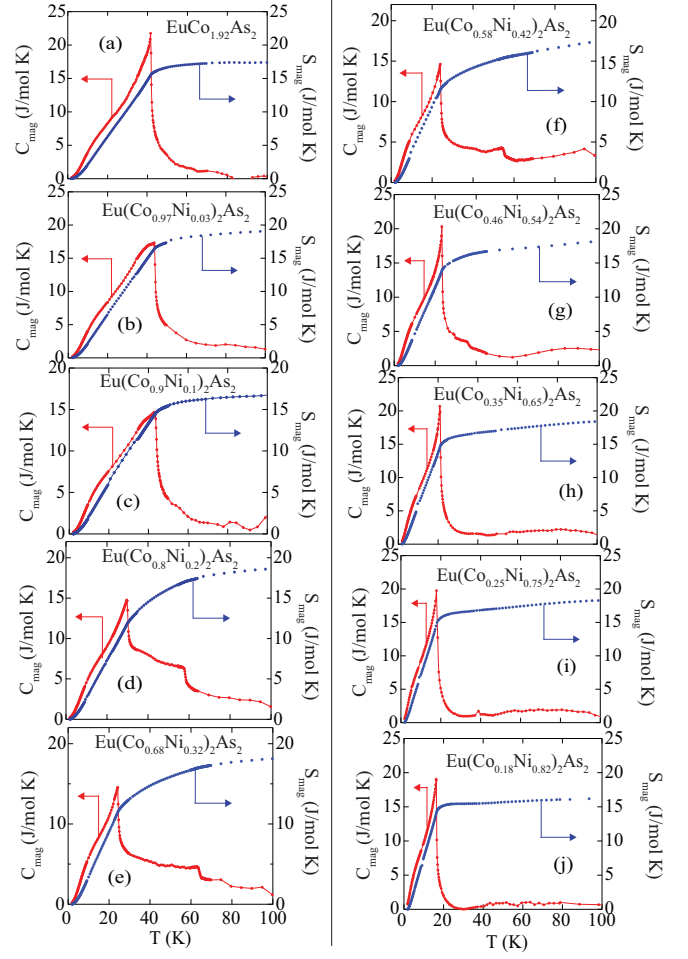


FIG. 24: Temperature T -dependent magnetic contribution $C_{\text{mag}}(T)$ obtained by subtracting the nonmagnetic contribution $C_p(T)$ of BaCo_2As_2 (left-hand ordinates) and the magnetic entropy $S_{\text{mag}}(T)$ calculated from the experimental $C_{\text{mag}}(T)/T$ data using Eq. (9) for $\text{Eu}(\text{Co}_{1-x}\text{Ni}_x)_{2-y}\text{As}_2$ (right-hand ordinates) for $x = 0, 0.03, 0.10, 0.20, 0.32, 0.42, 0.54, 0.65, 0.75$, and 0.82 from 1.8 to 100 K. The sharp λ -like transitions are associated with AFM ordering of the Eu spins and the steplike features for $x = 0.2$ – 0.54 are associated with itinerant FM ordering associated with the Co/Ni sublattice.

value, which may be due to a small error in estimating the lattice contribution to $C_p(T)$.

The $C_p(H, T)$ data for $\text{Eu}(\text{Co}_{1-x}\text{Ni}_x)_{2-y}\text{As}_2$ crystals with compositions $x = 0.2, 0.32, 0.42$, and 0.54 showing two magnetic transitions measured in magnetic fields $H = 0$ and $H = 3 \text{ T}$ applied along the c axis are shown in Fig. 25. It is evident that both transitions are intrinsic and magnetic because $T_{N\text{Eu}}$ shifts to lower temperatures marked by an arrow and the heat capacity jump at $T_{N\text{Eu}}$ decreases with applied magnetic field, both as predicted from MFT for a field parallel to the helix axis [36]. The second transition at $T_{C\text{Co/Ni}}$ as listed in Table II is seen to be suppressed by an applied field of 3 T. We take $T_{N\text{Eu}}$ at each field to be the temperature of the peak in C_p versus T instead of the temperature at half-

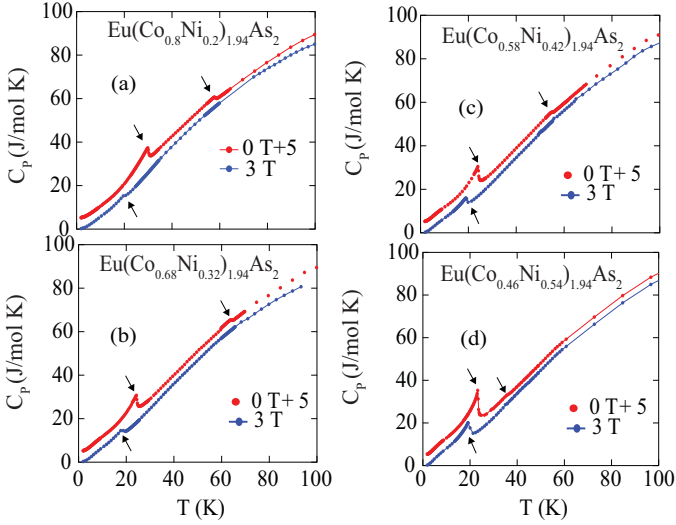


FIG. 25: Heat capacity C_p versus temperature T of $\text{Eu}(\text{Co}_{1-x}\text{Ni}_x)_2\text{As}_2$ with $x = 0.20, 0.32, 0.42$, and 0.54 in magnetic fields $H = 0$ and 3 T applied parallel to the c axis, $H \parallel c$. For clarity, the data for $H = 0$ T are offset by 5 J/mol K as indicated. Phase transitions are marked by arrows.

height of the transition, because the latter is ambiguous to estimate due to the significant contribution of short-range AFM ordering to C_p above the respective T_{NEu} . Table II lists the x -dependent T_{NEu} and $T_{\text{CCo/Ni}}$ values obtained from the $\chi(T)$ and $C_p(T)$ measurements and from the $\rho(T)$ measurements discussed in the following section. The values obtained from the different measurements are quite close to each other. The table shows that the $C_p(T)$ measurements do not reveal two transitions for $x = 0.65$ even though the two transitions are evident in both the $\chi(T)$ and $\rho(T)$ (see below) measurements.

VIII. ELECTRICAL RESISTIVITY

The in-plane (ab -plane) electrical resistivity ρ of the $\text{Eu}(\text{Co}_{1-x}\text{Ni}_x)_2\text{As}_2$ single crystals as a function of T from 1.8 to 300 K measured at zero magnetic field are shown in Fig. 26. The $\rho(T)$ exhibits metallic behavior for all crystals. The AFM transition at T_{NEu} and the second transition $T_{\text{CCo/Ni}}$ for $x = 0.32, 0.42$ and 0.54 observed in the $\rho(T)$ data are marked by arrows. The transitions are more clearly shown in the expanded plots of $\rho(T)$ at low temperatures in the insets to Fig. 26. The values of T_{N} and $T_{\text{CCo/Ni}}$ obtained from the data are listed in Table II and are seen to be consistent with the values found from the above $\chi(T)$ data and $C_p(T)$ measurements. Interestingly, the $\rho(T)$ data do not exhibit any significant feature at T_{NEu} for $x = 0.20$ and 0.65 .

The low- T $\rho_{ab}(T)$ data below T_{NEu} are fitted by

$$\rho(T) = \rho_0 + AT^n, \quad (10)$$

as shown by the solid curves in the insets of Fig. 26.

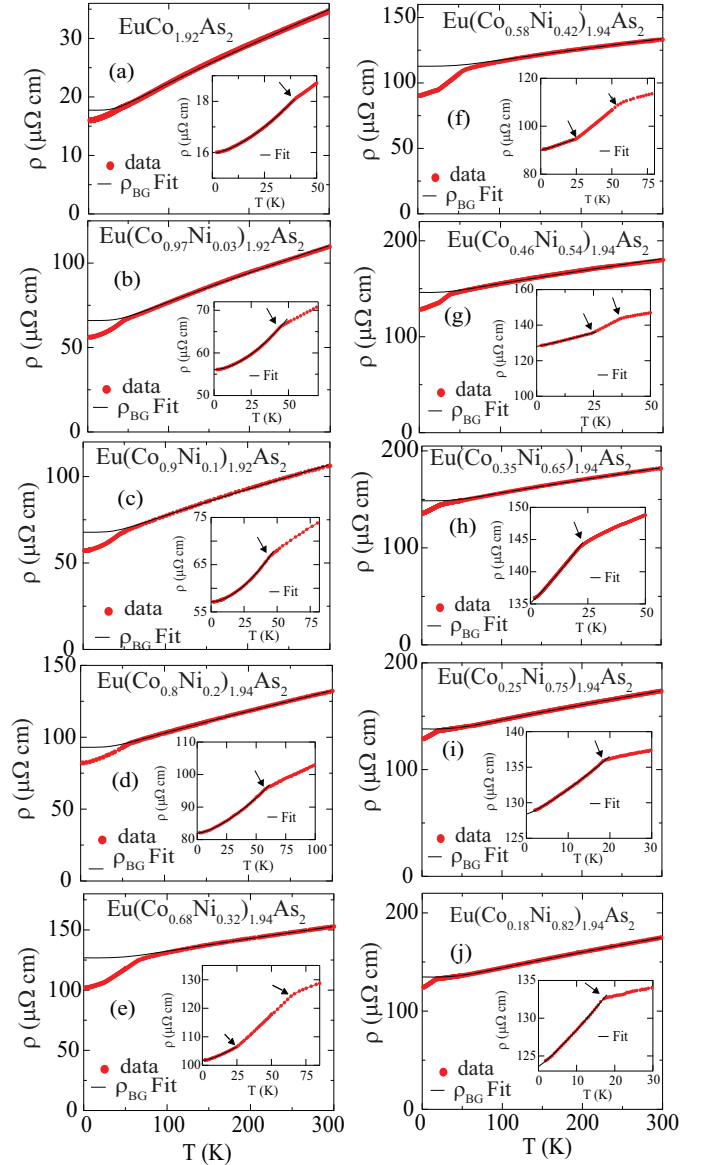


FIG. 26: In-plane electrical resistivity of $\text{Eu}(\text{Co}_{1-x}\text{Ni}_x)_2\text{As}_2$ single crystals ($x = 0, 0.03, 0.10, 0.20, 0.32, 0.42, 0.54, 0.65, 0.75$, and 0.82) as a function of temperature T from 1.8 to 300 K measured in zero magnetic field. The black curves in the main panels are fits by the prediction of the Bloch-Grüneisen theory in Eqs. (11) to the data above 70 K and are extrapolated to $T = 0$. Insets: Expanded plots of $\rho(T)$ at low T . The black line is the fit of the data by Eq. (10) over the temperature interval below $\min(T_{\text{CCo/Ni}}, T_{\text{NEu}})$ marked by an arrow.

The fitted parameters ρ_0 , A , and the power n are listed in Table VIII. From Table VIII, the $\rho(T)$ data follow the Fermi-liquid T^2 behavior for $x = 0$, but with doping $\rho(T \leq T_{\text{N}})$ does not, likely because it is affected by the T -dependent loss of spin-disorder scattering on cooling below T_{NEu} .

The $\rho(T)$ in the normal state above 70 K is fitted by the Bloch-Grüneisen (BG) model where the resistivity arises

TABLE VIII: Parameters for the electrical resistivity obtained from a low-temperature fit by Eq. (10) below $T_{\text{N Eu}}$ and for the fit by the Bloch-Grüneisen model in Eqs. (11) in the range $70 \text{ K} \leq T \leq 300 \text{ K}$.

x	Low- T , T^n fit			Bloch-Grüneisen fit		
	ρ_0 ($\mu\Omega \text{ cm}$)	A ($\mu\Omega \text{ cm/K}^n$)	n	$\rho_0 + \rho_{\text{sd}}$ ($\mu\Omega \text{ cm}$)	C ($\mu\Omega \text{ cm}$)	Θ_R (K)
0	16.0	0.0022(1)	2	17.7(3)	12(1)	213(3)
0.03	56.07(1)	0.0127(3)	1.75(1)	65(1)	37(3)	246(8)
0.1	57.11(1)	0.0115(1)	1.77(1)	67(1)	32(4)	256(9)
0.2	81.96(3)	0.0289(1)	1.52(1)	93.0(5)	31(2)	245(7)
0.32	101.63(3)	0.0581(6)	1.38(3)	126(2)	27(9)	319(6)
0.42	89.97(4)	0.14(1)	1.11(2)	112(3)	21(4)	311(8)
0.54	128.03(3)	0.21(1)	1.12(1)	146(1)	26(5)	228(9)
0.65	135.17(2)	0.30(1)	1.10(1)	148(1)	29(6)	266(6)
0.75	128.41(3)	0.21(1)	1.22(1)	138.0(3)	32(1)	271(5)
0.82	123.63(4)	0.34(1)	1.15(1)	134.7(2)	37.8(9)	282(7)
1	8.71(3)	0.262(9)	1.26(1)	17.18(3)	27.0(2)	235(1)

from scattering of electrons from acoustic phonons. Our fitting function is

$$\rho_{\text{BG}}(T) = \rho_0 + \rho_{\text{sd}}(T) + C f(T), \quad (11a)$$

where [63]

$$f(T) = \left(\frac{T}{\Theta_R} \right)^5 \int_0^{\Theta_R/T} \frac{x^5 dx}{(1 - e^{-x})(e^x - 1)} dx. \quad (11b)$$

Here $\rho_0 + \rho_{\text{sd}}(T)$ is the sum of the residual resistivity ρ_0 due to static defects in the crystal lattice and the spin-disorder resistivity $\rho_{\text{sd}}(T)$. The constant C describes the T -independent interaction strength of the conduction electrons with the thermally excited phonons and contains the ionic mass, Fermi velocity, and other parameters, $x = \frac{\hbar\omega}{2\pi k_{\text{B}}T}$, and Θ_R is the Debye temperature determined from electrical resistivity data. The representation of $f(T)$ used here is a fit of data calculated for the integral on the right-hand side of Eq. (11b) by an accurate analytic Padé approximant function of T [63]. The fits to the $\rho(T)$ data between 70 and 300 K by Eqs. (11) are shown as the solid black curves in the main panel of Fig. 26. The fitted parameters ($\rho_0 + \rho_{\text{sd}}$), C , and Θ_R are listed in Table VIII.

IX. CONCLUDING REMARKS

Multiple magnetic phase transitions have been identified in the $\text{Eu}(\text{Co}_{1-x}\text{Ni}_x)_{2-y}\text{As}_2$ system. The highest-temperature one is a composition-dependent itinerant FM ordering between 25 and 60 K associated with the Co/Ni sublattice as clearly revealed from both heat capacity $C_p(H, T)$ and magnetic susceptibility $\chi_\alpha(T)$ measurements. This FM transition is fragile and disappears in a 3 T magnetic field according to the $C_p(T)$ measurements. The composition-dependent magnetic ordering of

the Eu spins is clearly evident from the λ - or step-shape anomaly in the zero-field $C_p(T)$ measurements that is easily tracked versus composition. Close to the end-point compositions the magnetic structure is a c -axis helix as illustrated generically in Fig. 27 for a 60° turn angle kd . In the intermediate composition range $0.20 \leq x \leq 0.65$, low-field magnetization versus field $M_\alpha(H)$ isotherms demonstrate that the Eu magnetic structure has a rather large ferromagnetic (FM) component along the c axis (0.6 to $3.5 \mu_{\text{B}}/\text{Eu}$); combined with the $\chi_\alpha(T)$ data, we suggest that this structure is an Eu $S = 7/2$ cone structure, which is a superposition of an c -axis helix and a c -axis FM component as illustrated in Fig. 27(b). In addition, in the narrow composition range $0.03 \lesssim x \lesssim 0.1$ there appears to be a $2q$ helix, which consists of a superposition of a helical structure along the c axis with the moments aligned in the ab plane and a related helix structure with an axis in the ab plane and the moments aligned in an ab - c plane perpendicular to the helix axis. These results are summarized in the tentative phase diagram in Fig. 28.

The most surprising result from this work is the discovery of multiple transition temperatures around the Eu transition temperature that are observed in the ^{151}Eu Mössbauer measurements of $\text{Eu}(\text{Co}_{1-x}\text{Ni}_x)_{2-y}\text{As}_2$ with $x = 0, 0.2$, and 0.65 , which are not included in Fig. 28. These measurements indicate that ordering of the Eu moments proceeds via an incommensurate sine amplitude-modulated structure with additional transition temperatures associated with this effect. A fit of the ordered moment versus temperature in $\text{EuCo}_{2-y}\text{As}_2$ from the literature suggests that there might be a systematic deviation from the prediction of molecular-field theory on approaching $T_{\text{N Eu}}$ from below, which is expected to be accurate for the large spin $S = 7/2$. It would be interesting to carry out higher-resolution measurements of the magnetic order parameter versus temperature for $x = 0$, and also see if there is a temperature dependence to the

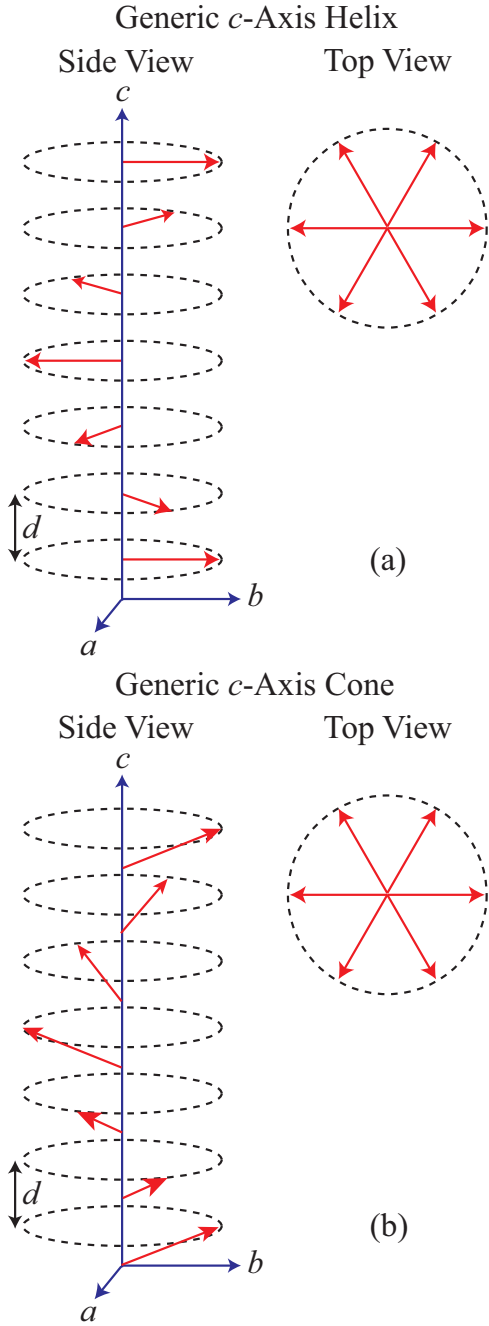


FIG. 27: (a) Generic magnetic structure of a c -axis helix, which consists of ferromagnetically (FM)-aligned moments in the ab plane represented by a single arrow which rotates by an angle $q_c d$ from layer to layer along the c axis, where q_c is the c -axis magnetic propagation vector and d is the distance between adjacent ab planes of FM-aligned moments as shown (after Ref. [35]). (b) Generic c -axis cone structure consisting of a superposition of a c -axis helix structure and a c -axis FM component of each moment.

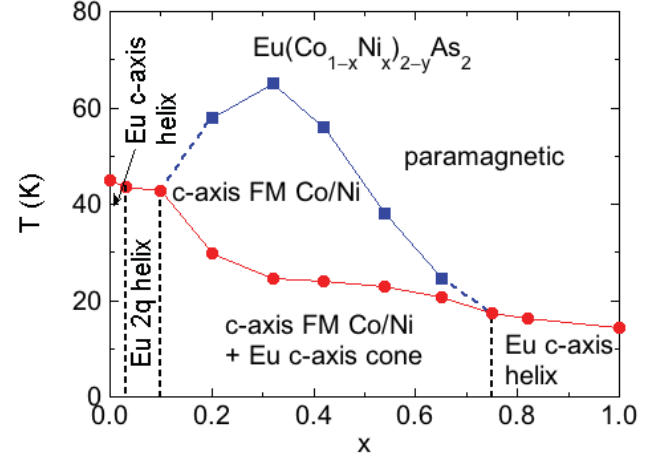


FIG. 28: Tentative magnetic phase diagram in the T - x plane of the $\text{Eu}(\text{Co}_{1-x}\text{Ni}_x)_{2-y}\text{As}_2$ system. The itinerant FM transition temperatures $T_{C\text{Co/Ni}}$ of the Co/Ni sublattice are given by the filled blue squares, and the AFM helical local-moment transition temperatures $T_{N\text{Eu}}$ of the Eu spins are denoted by filled red circles.

turn angle of the helix at this composition.

Acknowledgments

This research was supported by the U.S. Department of Energy, Office of Basic Energy Sciences, Division of Materials Sciences and Engineering. Ames Laboratory is operated for the U.S. Department of Energy by Iowa State University under Contract No. DE-AC02-07CH11358. Financial support for this work was provided by Fonds Québécois de la Recherche sur la Nature et les Technologies. Much of the Mössbauer work was carried out while DHR was on sabbatical leave at Iowa State University and Ames Laboratory and their generous support (again under contract No. DE-AC02-07CH11358) during this visit is gratefully acknowledged.

- [1] D. C. Johnston, The puzzle of high temperature superconductivity in layered iron pnictides and chalcogenides, *Adv. Phys.* **59**, 803 (2010).
- [2] P. C. Canfield and S. L. Bud'ko, FeAs-Based Superconductivity: A Case Study of the Effects of Transition Metal Doping on BaFe_2As_2 , *Annu. Rev. Condens. Matter Phys.* **1**, 27 (2010).
- [3] G. R. Stewart, Superconductivity in iron compounds, *Rev. Mod. Phys.* **83**, 1589 (2011).
- [4] D. J. Scalapino, A common thread: The pairing interaction for unconventional superconductors, *Rev. Mod. Phys.* **84**, 1383 (2012).
- [5] R. M. Fernandes, A. V. Chubukov, and J. Schmalian, What drives nematic order in iron-based superconductors?, *Nat. Phys.* **10**, 97 (2014).
- [6] P. Dai, Antiferromagnetic order and spin dynamics in iron-based superconductors, *Rev. Mod. Phys.* **87**, 855 (2015).
- [7] D. S. Inosov, Spin fluctuations in iron pnictides and chalcogenides: From antiferromagnetism to superconductivity, *Compt. Rend. Phys.* **17**, 60 (2016).
- [8] Q. Si, R. Yu, and E. Abrahams, High-temperature superconductivity in iron pnictides and chalcogenides, *Nat. Rev. Mater.* **1**, 16017 (2016).
- [9] M. Pfisterer and G. Nagorsen, On the Structure of Ternary Arsenides, *Z. Naturforsch.* **35b**, 703 (1980).
- [10] M. Pfisterer and G. Nagorsen, Bonding and Magnetic Properties in Ternary Arsenides ET_2As_2 , *Z. Naturforsch.* **38b**, 811 (1983).
- [11] Y. Singh, A. Ellern, and D. C. Johnston, Magnetic, transport, and thermal properties of single crystals of the layered arsenide BaMn_2As_2 , *Phys. Rev. B* **79**, 094519 (2009).
- [12] A. Pandey, R. S. Dhaka, J. Lamsal, Y. Lee, V. K. Anand, A. Kreyssig, T. W. Heitmann, R. J. McQueeney, A. I. Goldman, B. N. Harmon, A. Kaminski, and D. C. Johnston, $\text{Ba}_{1-x}\text{K}_x\text{Mn}_2\text{As}_2$: An Antiferromagnetic Local-Moment Metal, *Phys. Rev. Lett.* **108**, 087005 (2012).
- [13] V. K. Anand, R. S. Dhaka, Y. Lee, B. N. Harmon, A. Kaminski, and D. C. Johnston, Physical properties of metallic antiferromagnetic $\text{CaCo}_{1.86}\text{As}_2$ single crystals, *Phys. Rev. B* **89**, 214409 (2014).
- [14] D. J. Singh, A. S. Sefat, M. A. McGuire, B. C. Sales, D. Mandrus, L. H. VanBebber, and V. Keppens, Itinerant antiferromagnetism in BaCr_2As_2 : Experimental characterization and electronic structure calculations, *Phys. Rev. B* **79**, 094429 (2009).
- [15] N. S. Sangeetha, A. Pandey, Z. A. Benson, and D. C. Johnston, Strong magnetic correlations to 900 K in single crystals of the trigonal antiferromagnetic insulators SrMn_2As_2 and CaMn_2As_2 , *Phys. Rev. B* **94**, 094417 (2016).
- [16] P. Das, N. S. Sangeetha, A. Pandey, Z. A. Benson, T. W. Heitmann, D. C. Johnston, A. I. Goldman, and A. Kreyssig, Collinear antiferromagnetism in trigonal SrMn_2As_2 revealed by single-crystal neutron diffraction, *J. Phys.: Condens. Matter* **29**, 035802 (2017).
- [17] W. T. Jayasekara, A. Pandey, A. Kreyssig, N. S. Sangeetha, A. Sapkota, K. Kothapalli, V. K. Anand, W. Tian, D. Vaknin, D. C. Johnston, R. J. McQueeney, A. I. Goldman, and B. G. Ueland, Suppression of magnetic order in $\text{CaCo}_{1.86}\text{As}_2$ with Fe substitution: Magnetization, neutron diffraction, and x-ray diffraction studies of $\text{Ca}(\text{Co}_{1-x}\text{Fe}_x)_y\text{As}_2$, *Phys. Rev. B* **95**, 064425 (2017).
- [18] A. Pandey, D. G. Quirinale, W. Jayasekara, A. Sapkota, M. G. Kim, R. S. Dhaka, Y. Lee, T. W. Heitmann, P. W. Stephens, V. Ogloblichev, A. Kreyssig, R. J. McQueeney, A. I. Goldman, A. Kaminski, B. N. Harmon, Y. Furukawa, and D. C. Johnston, Crystallographic, electronic, thermal, and magnetic properties of single-crystal SrCo_2As_2 , *Phys. Rev. B* **88**, 014526 (2013).
- [19] N. S. Sangeetha, V. Smetana, A.-V. Mudring, and D. C. Johnston, Antiferromagnetism in semiconducting SrMn_2Sb_2 and BaMn_2Sb_2 single crystals, *Phys. Rev. B* **97**, 014402 (2018).
- [20] N. S. Sangeetha, V. Smetana, A.-V. Mudring, and D. C. Johnston, Anomalous Composition-Induced Crossover in the Magnetic Properties of the Itinerant-Electron Antiferromagnet $\text{Ca}_{1-x}\text{Sr}_x\text{Co}_{2-y}\text{As}_2$, *Phys. Rev. Lett.* **119**, 257203 (2017).
- [21] P. Das, N. S. Sangeetha, G. R. Lindemann, T. W. Heitmann, A. Kreyssig, A. I. Goldman, R. J. McQueeney, D. C. Johnston, and D. Vaknin, Itinerant G-type antiferromagnetic order in SrCr_2As_2 , *Phys. Rev. B* **96**, 014411 (2017).
- [22] R. Marchand and W. Jeitschko, Ternary lanthanoid-transition metal pnictides with ThCr_2Si_2 -type structure, *J. Solid State Chem.* **24**, 351 (1978).
- [23] Y. Xiao, Y. Su, M. Meven, R. Mittal, C. M. N. Kumar, T. Chatterji, S. Price, J. Persson, N. Kumar, S. K. Dhar, A. Thamizhavel, and Th. Brueckel, Magnetic structure of EuFe_2As_2 determined by single-crystal neutron diffraction, *Phys. Rev. B* **80**, 174424 (2009).
- [24] H. S. Jeevan, Z. Hossain, D. Kasinathan, H. Rosner, C. Geibel, and P. Gegenwart, Electrical resistivity and specific heat of single-crystalline EuFe_2As_2 : A magnetic homologue of SrFe_2As_2 , *Phys. Rev. B* **78**, 052502 (2008).
- [25] Z. Ren, Q. Tao, S. Jiang, C. Feng, C. Wang, J. Dai, G. Cao, and Z. Xu, Superconductivity Induced by Phosphorus Doping and Its Coexistence with Ferromagnetism in $\text{EuFe}_2(\text{As}_{0.7}\text{P}_{0.3})_2$, *Phys. Rev. Lett.* **102**, 137002 (2009).
- [26] S. Jiang, H. Xing, G. Xuan, Z. Ren, C. Wang, Z. A. Xu, and G. Cao, Superconductivity and local-moment magnetism in $\text{Eu}(\text{Fe}_{0.89}\text{Co}_{0.11})_2\text{As}_2$, *Phys. Rev. B* **80**, 184514 (2009).
- [27] C. F. Miclea, M. Nicklas, H. S. Jeevan, D. Kasinathan, Z. Hossain, H. Rosner, P. Gegenwart, C. Geibel, and F. Steglich, Evidence for a reentrant superconducting state in EuFe_2As_2 under pressure, *Phys. Rev. B* **79**, 212509 (2009).
- [28] H. S. Jeevan, D. Kasinathan, H. Rosner, and P. Gegenwart, Interplay of antiferromagnetism, ferromagnetism, and superconductivity in $\text{EuFe}_2(\text{As}_{1-x}\text{P}_x)_2$ single crystals, *Phys. Rev. B* **83**, 054511 (2011).
- [29] For a review of cT and uCT structures in pnictides, see V. K. Anand, P. Kanchana-Perera, A. Pandey, R. J. Goetsch, A. Kreyssig, and D. C. Johnston, Crystal growth and physical properties of SrCu_2As_2 , SrCu_2Sb_2 , and BaCu_2Sb_2 , *Phys. Rev. B* **85**, 214523 (2012).
- [30] E. Mörsen, B. D. Mosel, W. Müller-Warmuth, M. Reehuis, and W. Jeitschko, Mössbauer and Magnetic Susceptibility Investigations of Strontium, Lanthanum and

- Europium Transition Metal Phosphides with ThCr_2Si_2 Type Structure, *J. Phys. Chem. Solids* **49**, 785 (1988).
- [31] M. Reehuis, W. Jeitschko, M. H. Möller, and P. J. Brown, A Neutron Diffraction Study of the Magnetic Structure of EuCo_2P_2 , *J. Phys. Chem. Solids* **53**, 687 (1992).
- [32] C. Huhnt, W. Schlabit, A. Würth, A. Mewis, and M. Reehuis, First-order phase transitions in EuCo_2P_2 and SrNi_2P_2 , *Phys. Rev. B* **56**, 13796 (1997).
- [33] M. Chefki, M. M. Abd-Elmeguid, H. Micklitz, C. Huhnt, W. Schlabit, M. Reehuis, and W. Jeitschko, Pressure-Induced Transition of the Sublattice Magnetization in EuCo_2P_2 : Change from Local Moment $\text{Eu}(4f)$ to Itinerant $\text{Co}(3d)$ Magnetism, *Phys. Rev. Lett.* **80**, 802 (1998).
- [34] N. S. Sangeetha, E. Cuervo-Reyes, A. Pandey, and D. C. Johnston, EuCo_2P_2 : A model molecular-field helical Heisenberg antiferromagnet, *Phys. Rev. B* **94**, 014422 (2016).
- [35] D. C. Johnston, Magnetic Susceptibility of Collinear and Noncollinear Heisenberg Antiferromagnets, *Phys. Rev. Lett.* **109**, 077201 (2012).
- [36] D. C. Johnston, Unified molecular field theory for collinear and noncollinear Heisenberg antiferromagnets, *Phys. Rev. B* **91**, 064427 (2015).
- [37] H. Raffius, E. Mörsen, B. D. Mosel, W. Müller-Warmuth, W. Jeitschko, L. Terbüchte, and T. Vomhof, Magnetic properties of ternary lanthanoid transition metal arsenides studied by Mössbauer and susceptibility measurements, *J. Phys. Chem. Solids* **54**, 135 (1993).
- [38] M. Bishop, W. Uchoy, G. Tsoi, Y. K. Vohra, A. S. Sefat, and B. C. Sales, Formation of collapsed tetragonal phase in $\text{EuCo}_{2-y}\text{As}_2$, *J. Phys.: Condens. Matter* **22**, 425701 (2010).
- [39] J. Ballinger, L. E. Wenger, Y. K. Vohra, and A. S. Sefat, Magnetic properties of single crystal $\text{EuCo}_{2-y}\text{As}_2$, *J. Appl. Phys.* **111**, 07E106 (2012).
- [40] X. Tan, G. Fabbri, D. Haskel, A. A. Yaroslavtsev, H. Cao, C. M. Thompson, K. Kovnir, A. P. Penushenkov, R. V. Chernikov, V. O. Garlea, and M. Shatruk, A Transition from Localized to Strongly Correlated Electron Behavior and Mixed Valence Driven by Physical or Chemical Pressure in ACo_2As_2 ($A = \text{Eu}$ and Ca), *J. Am. Chem. Soc.* **138**, 2724 (2016).
- [41] N. S. Sangeetha, V. K. Anand, E. Cuervo-Reyes, V. Smetana, A.-V. Mudring and D. C. Johnston, Enhanced moments of Eu in single crystals of the metallic helical antiferromagnet $\text{EuCo}_{2-y}\text{As}_2$, *Phys. Rev. B* **97**, 144403 (2018).
- [42] Q.-P. Ding, N. Higa, N. S. Sangeetha, D. C. Johnston, and Y. Furukawa, NMR determination of an incommensurate helical antiferromagnetic structure in EuCo_2As_2 , *Phys. Rev. B* **95**, 184404 (2017).
- [43] E. H. El Ghadraoui, J. Y. Pivan, R. Guérin, O. Pena, J. Padiou, and M. Sergent, Polymorphism and Physical Properties of LnNi_2As_2 Compounds ($\text{Ln} = \text{La} \rightarrow \text{Gd}$), *Mater. Res. Bull.* **23**, 1345 (1988).
- [44] E. D. Bauer, F. Ronning, B. L. Scott, and J. D. Thompson, Superconductivity in SrNi_2As_2 crystals, *Phys. Rev. B* **78**, 172504 (2008).
- [45] W. T. Jin, N. Qureshi, Z. Bukowski, Y. Xiao, S. Nandi, M. Babij, Z. Fu, Y. Su, and Th. Brückel, Spiral magnetic ordering of the Eu moments in EuNi_2As_2 , *Phys. Rev. B* **99**, 014425 (2019).
- [46] N. S. Sangeetha, V. Smetana, A.-V. Mudring, and D. C. Johnston, Helical antiferromagnetic ordering in $\text{EuNi}_{1.95}\text{As}_2$ single crystals, *Phys. Rev. B* **100**, 094438 (2019).
- [47] APEX3, Bruker AXS Inc., Madison, Wisconsin, USA, 2015.
- [48] SAINT, Bruker AXS Inc., Madison, Wisconsin, USA, 2015.
- [49] L. Krause, R. Herbst-Irmer, G. M. Sheldrick, and D. J. Stalke, Comparison of silver and molybdenum microfocus X-ray sources for single-crystal structure determination, *Appl. Crystallogr.* **48**, 3 (2015).
- [50] G. M. Sheldrick, SHELTX – Integrated space-group and crystal-structure determination, *Acta Crystallogr. A* **71**, 3 (2015).
- [51] G. M. Sheldrick, Crystal structure refinement with SHELXL, *Acta Crystallogr. C* **71**, 3 (2015).
- [52] J. Rodríguez-Carvajal, Recent advances in magnetic structure determination by neutron powder diffraction, *Physica B* **192**, 55 (1993).
- [53] C. J. Voyer and D. H. Ryan, A complete solution to the Mössbauer problem all in one place, *Hyperfine Interact.* **170**, 91 (2006).
- [54] N. S. Sangeetha, L.-L. Wang, A. V. Smirnov, V. Smetana, A.-V. Mudring, D. D. Johnson, M. A. Tanatar, R. Prozorov, and D. C. Johnston, Non-Fermi-liquid behaviors associated with a magnetic quantum-critical point in $\text{Sr}(\text{Co}_{1-x}\text{Ni}_x)_2\text{As}_2$ single crystals, *Phys. Rev. B* **100**, 094447 (2019).
- [55] M. E. Fisher, Relation between the specific heat and susceptibility of an antiferromagnet, *Phil. Mag.* **7**, 1731 (1962).
- [56] D. C. Johnston, Magnetic dipole interactions in crystals, *Phys. Rev. B* **93**, 014421 (2016).
- [57] D. C. Johnston, Influence of uniaxial single-ion anisotropy on the magnetic and thermal properties of Heisenberg antiferromagnets within unified molecular field theory, *Phys. Rev. B* **95**, 094421 (2017).
- [58] P. Bonville, J. A. Hodges, M. Shirakawa, M. Kasaya, and D. Schmitt, Incommensurate modulated magnetic structure in orthorhombic EuPdSb , *Eur. Phys. J. B* **21**, 349 (2001).
- [59] A. Maurya, P. Bonville, A. Thamizhavel, and S. K. Dhar, EuNiGe_3 , an anisotropic antiferromagnet, *J. Phys.: Condens. Matter* **26**, 216001 (2014).
- [60] D. H. Ryan, A. Legros, O. Niehaus, R. Pöttgen, J. M. Cadogan, and R. Flacau, Modulated ferromagnetic ordering and the magnetocaloric response of Eu_4PdMg , *J. Appl. Phys.* **117**, 17D108 (2015).
- [61] J. A. Blanco, D. Gignoux, and D. Schmitt, Specific heat in some gadolinium compounds. II. Theoretical model, *Phys. Rev. B* **43**, 13145 (1991).
- [62] M. Rotter, M. Loewenhaupt, M. Doerr, A. Lindbaum, and H. Michor, Nonlinear amplitude-modulated magnetic order in Gd compounds, *Phys. Rev. B* **64**, 014402 (2001).
- [63] R. J. Goetsch, V. K. Anand, A. Pandey, and D. C. Johnston, Structural, thermal, magnetic, and electronic transport properties of the $\text{LaNi}_2(\text{Ge}_{1-x}\text{P}_x)_2$ system, *Phys. Rev. B* **85**, 054517 (2012).